Southern Ocean low cloud and precipitation phase observed during the Macquarie Island Cloud and Radiation Experiment (MICRE)

Emily Tansey[1], Roger T Marchand[1], Simon Peter Alexander[2], Andrew R. Klekociuk[2], and Alain Protat[3]

[1]University of Washington
[2]Australian Antarctic Division
[3]Australian Bureau of Meteorology

May 13, 2023

Abstract

Shallow cloud decks residing in or near the boundary layer cover a large fraction of the Southern Ocean (SO) and play a major role in determining the amount of shortwave radiation reflected back to space from this region. In this article, we examine the macrophysical characteristics and thermodynamic phase of low clouds (tops < 3 km) and precipitation using ground-based ceilometer, depolarization lidar and vertically-pointing W-band radar measurements collected during the Macquarie Island Cloud and Radiation Experiment (MICRE) from April 2016-March 2017. During MICRE, low clouds occurred ~65% of the time on average (slightly more often in austral winter than summer). About 2/3 of low clouds were cold-topped (temperatures < 0°C); these were thicker and had higher bases on average than warm-topped clouds. 83-88% of cold-topped low clouds were liquid phase at cloud base (depending on the season). The majority of low clouds had precipitation in the vertical range 150 to 250 meters below cloud base, a significant fraction of which did not reach the surface. Phase characterization is limited to the period between April 2016 and November 2016. Small-particle (low-radar-reflectivity) precipitation (which dominates precipitation occurrence) was mostly liquid below-cloud, while large-particle precipitation (which dominates total accumulation) was predominantly mixed/ambiguous or ice phase. Approximately 40% of cold-topped clouds had mixed/ambiguous or ice phase precipitation below (with predominantly liquid phase cloud droplets at cloud base). Below-cloud precipitation with radar reflectivity factors below about -10 dBZ were predominantly liquid, while reflectivity factors above about 0 dBZ were predominantly ice.

Hosted file

`962601_0_art_file_10974061_rppppl.docx` available at https://authorea.com/users/617006/articles/642674-southern-ocean-low-cloud-and-precipitation-phase-observed-during-the-macquarie-island-cloud-and-radiation-experiment-micre

Southern Ocean low cloud and precipitation phase observed during the Macquarie Island Cloud and Radiation Experiment (MICRE)

Emily Tansey[1], Roger Marchand[1], Simon P. Alexander[2,3], Andrew R. Klekociuk[2,3], and Alain Protat[2,4]

[1]University of Washington, Seattle, Washington, United States
[2]Australian Antarctic Division, Hobart, TAS, Australia
[3]Australian Antarctic Partnership Program, Institute for Marine and Antarctic Studies, University of Tasmania, Hobart, TAS, Australia
[4]Australian Bureau of Meteorology, Melbourne, Victoria, Australia

Corresponding author: Emily Tansey (etansey@uw.edu)

Key Points:

- Ground observations at Macquarie Island indicate that low clouds occur ~65% of the time; the majority have cloud top temperatures below 0°C.
- ~85% of low clouds with top temperatures < 0°C have liquid-phase bases and form precipitation, much of which does not reach the surface.
- Liquid-phase precipitation directly below cloud base had radar reflectivities < -10 dBZ; reflectivities above 0 dBZ were predominantly ice.

Abstract

Shallow cloud decks residing in or near the boundary layer cover a large fraction of the Southern Ocean (SO) and play a major role in determining the amount of shortwave radiation reflected back to space from this region. In this article, we examine the macrophysical characteristics and thermodynamic phase of low clouds (tops < 3 km) and precipitation using ground-based ceilometer, depolarization lidar and vertically-pointing W-band radar measurements collected during the Macquarie Island Cloud and Radiation Experiment (MICRE) from April 2016-March 2017. During MICRE, low clouds occurred ~65% of the time on average (slightly more often in austral winter than summer). About 2/3 of low clouds were cold-topped (temperatures < 0°C); these were thicker and had higher bases on average than warm-topped clouds. 83-88% of cold-topped low clouds were liquid phase at cloud base (depending on the season). The majority of low clouds had precipitation in the vertical range 150 to 250 meters below cloud base, a significant fraction of which did not reach the surface. Phase characterization is limited to the period between April 2016 and November 2016. Small-particle (low-radar-reflectivity) precipitation (which dominates precipitation occurrence) was mostly liquid below-cloud, while large-particle precipitation (which dominates total accumulation) was predominantly mixed/ambiguous or ice phase. Approximately 40% of cold-topped clouds had mixed/ambiguous or ice phase precipitation below (with predominantly liquid phase cloud droplets at cloud base). Below-cloud precipitation with radar reflectivity factors below about -10 dBZ were predominantly liquid, while reflectivity factors above about 0 dBZ were predominantly ice.

Plain Language Summary

The Southern Ocean is covered by low altitude cloud decks the majority of the time. Properties like cloud occurrence frequency, particle phase and precipitation habits determine how much solar radiation clouds reflect and how much infrared radiation they emit, which in turn affects the balance of the planet's incoming and outgoing radiation. In this paper, we examine low cloud properties observed from the ground at Macquarie Island, including how frequently they occur and at what temperatures. We study particle thermodynamic phase (liquid, ice or mixed) at cloud base and in precipitation below-cloud. A majority of low clouds are predominantly composed of liquid phase droplets, although frozen precipitation is frequently found below cloud base. Low clouds form precipitation more often than not, much of which evaporates before reaching the ground. In below-freezing low clouds, the majority of large raindrops & snowflakes that do reach

the ground originate as frozen precipitation directly below cloud base. This indicates that ice formation is frequently active in clouds composed predominantly of liquid-phase droplets. Lastly, we build upon an established radar-lidar relationship that particles with radar reflectivity factors below -10 dBZ are generally liquid, whereas above 0 dBZ are most often ice phase.

1. Introduction

Shallow cloud decks residing in or near the boundary layer cover a large fraction of the Southern Ocean (SO) and play a major role in determining the amount of shortwave radiation reflected back to space from this region [Mace 2010, Bodas-Salcedo et al. 2016, Huang et al. 2016]. For many years now, models have struggled to simulate correctly top-of-atmosphere radiative fluxes and the surface energy budget of the SO [Trenberth & Fasullo 2010, Bodas-Salcedo et al. 2016, Schneider & Reusch 2016]. These radiative errors influence local and global atmospheric and oceanic circulations [Ceppi et al. 2012, 2013, Hwang & Frierson 2013, Sallée et al. 2013, Kay et al. 2016] and global climate sensitivity [Gettelman et al. 2019, Bodas-Salcedo et al. 2019, Zelinka et al. 2020]. The radiative bias is smaller on average in the current generation of climate models than in the previous generation (specifically, those participating in the Cloud Model Intercomparison Project phase 6 (CMIP6) relative to phase 5 (CMIP5)), but significant radiative bias remains [Schuddeboom & McDonald 2021, Cesana et al. 2022, Lauer et al. 2023, Mallet et al. 2023].

Satellite observations indicate that SO stratocumulus clouds (StCu) are predominantly composed of supercooled liquid, at least at cloud top [Huang et al. 2016, Mace et al. 2020, 2021a], and at least for CMIP5 models, several studies found that the radiative bias was related to the incorrect partitioning of the cloud phase (ice vs. liquid) in these shallow clouds, especially in cyclone cold sectors [Bodas-Salcedo et al. 2016, Kay et al. 2016, Frey & Kay, 2017]. While it remains to be seen to what degree phase partitioning is a dominant source of the remaining model radiative bias, it is clear that climate models need to capture well the temperature dependence of clouds (that is, cloud feedbacks) in this region. Zelinka et al. [2020], for example, found in a multi-climate-model analysis that low cloud feedbacks over the SO increased from weakly negative on average in CMIP5 to positive in CMIP6, yielding an overall global cloud feedback which is significantly more positive in CMIP6 (and consequently CMIP6 models have a larger climate sensitivity and greater warming on average). The low cloud feedback increased in CMIP6 because models contain more low-altitude liquid clouds and fewer ice clouds. This sensitivity of the cloud feedback to phase arises in models because liquid cloud cover and cloud albedo tend to reduce with warming (a positive cloud feedback), while ice clouds tend to melt to form brighter liquid clouds (a negative cloud feedback). There is reasonable observational support for this overall tendency [e.g., Terai et al 2019]. Nonetheless, low cloud macrophysical properties (such as cloud occurrence and thickness) as well as microphysical properties (such as liquid water content, effective radius and droplet number concentration) that ultimately control the cloud albedo are influenced by many factors including precipitation [Wood 2012].

Precipitation is very common in SO clouds [Wang et al. 2015, Tansey et al. 2022]. In liquid phase clouds, precipitation is associated with an increase in the effective radius and decrease in cloud liquid water path, both of which lower albedo [Ceppi et al. 2015]. In mixed phase clouds, the presence of ice phase particles substantially impacts the cloud microphysics because ice particles more readily uptake water vapor than liquid particles, growing into precipitation sized particles at the expense of water droplets (the Wegener–Bergeron–Findeisen process) [e.g. Fan et al. 2011]. Ice particles also grow efficiently by accreting liquid cloud droplets, creating rimed particles [Wood 2012]. Precipitation also removes aerosols (dusts and other particulate matter that can serve as cloud-condensation nuclei on which cloud droplets form) from the atmosphere, lowering the cloud droplet concentration [Wood 2012, McCoy et al. 2020]. In particular, Kang et al. [2022] have recently shown that coalescence of liquid cloud droplets (which initiates precipitation) is the primary process through which aerosols are removed from the boundary layer and plays an important (if not dominant) role in controlling droplet concentration in both liquid and mixed phase SO StCu. And of course, all of these microphysical changes can affect cloud lifetime and thereby the time-average cloud cover.

But how often are SO low clouds producing frozen or mix-phase precipitation? Based on ship data, Mace and Protat [2018] (hereafter MP18) show ice phase precipitation falls from SO StCu more often than spaceborne lidar suggest. Based on depolarization lidar observations from the ship-based Clouds, Aerosols, Precipitation, Radiation and Atmospheric Composition over the SO (CAPRICORN I) experiment in March and April 2016, MP18 found that between 20% and 40%

of cold-topped (< $0^{o}C$) SO StCu cloud layers were found to have ice or mixed-phase precipitation falling from their cloud base, while at the same time appearing to be overwhelmingly liquid phase (at cloud top) based on depolarization measurement by the Cloud-Aerosol Lidar and Infrared Pathfinder Satellite Observation (CALIPSO). MP18 (as well as a more detailed study by Mace [2020]) conclude that because visible photons are largely absorbed or backscattered within a few optical depths of cloud top, CALIPSO does not identify the presence of ice in the SO StCu because ice often exists deeper within the cloud. Consequently, measurements from the surface are essential to our understanding of cloud-base and below-cloud precipitation phase.

Few surface-based observational datasets exist across the SO that can be used to assess cloud and precipitation phase. One such dataset is the surface-based observational record from the Macquarie Island Cloud and Radiation Experiment (MICRE), which took place between March 2016 and March 2018 [Mcfarquhar et al. 2021]. Macquarie Island (54.5°S, 158.9°E) has a narrow isthmus at its northernmost tip where surface meteorology and tipping bucket rainfall data have been recorded by the Australian Bureau of Meteorology (BoM) since 1948. The station is situated in the middle of the SO storm track and is therefore a suitable location to observe SO cloud and precipitation systems carried by prevailing westerly winds. During MICRE, the U.S. Department of Energy Atmospheric Radiation Measurement (ARM) program, Australian Antarctic Division (AAD) and BoM collaboratively deployed ground instrumentation with the goal of measuring cloud, precipitation, and radiative characteristics. To date, MICRE surface radiation and surface precipitation properties have been analyzed in detail by Hinkelman & Marchand [2020] and Tansey et al. [2022], respectively. In this article we focus on cloud base and below-cloud precipitation phase, relying on the Vaisala CTK-25 ceilometer (905 nm; supplied by ARM), W-band cloud radar (supplied by BoM), and AAD polarization lidar (532 nm). Two Vaisala ceilometers were operating during MICRE, one deployed by ARM and one by the University of Canterbury. The instruments were concurrently available for the period of April-November 2016, providing us with some ability to comment on seasonal characteristics.

Section 2 of this paper outlines the MICRE data, retrievals and sources of uncertainty. Results are presented in section 3, organized in terms of basic cloud macrophysical characteristics at

Macquarie Island (section 3.1), cloud base phase (section 3.2), below-cloud precipitation phase (section 3.3), the relationship between radar dBZ and lidar depolarization ratios (section 3.4) and lastly, a comparison of lidar below-cloud properties to the blended surface precipitation data product of Tansey et al. [2022] (section 3.5). A summary and discussion is given in section 4.

2. Data and methods

Much of the analysis presented in this article is based on the determination of the cloud base phase and the phase of precipitation just below cloud base. Following a brief description of the measurements and the approach used to determine cloud boundaries in Section 2.1 and the lidar calibration in section 2.2, the techniques used to determine cloud-base and precipitation phase are given in section 2.3 and 2.4, respectively.

2.1 Cloud macrophysical characteristics: ceilometer, W-band radar and radiosondes

Basic cloud macrophysical properties (low cloud occurrence, number of low cloud layers, and cloud top and base temperatures) are determined using a combination of radiosonde temperature profiles, along with W-band cloud radar and laser ceilometers. Specifically, cloud base height (CBH) is determined using a Vaisala ceilometer [Münkel et al. 2007, Kuma et al. 2020], and cloud top heights (CTH) from a combination of W-band radar and ceilometer (details follow below). The radar, the Bistatic rAdar SysTem for Atmospheric studies (BASTA) [Delanoë et al. 2016], operated in several modes which have been merged to produce a time-height record of radar reflectivity and Doppler velocity on a 12-second-by-25-m time-height grid, with a minimum detectable signal (MDS) of about -40 dBZ at 1 km. The MDS is sufficient to detect essentially all precipitating clouds near the surface, but the radar does at times miss non-precipitating clouds that are detected by the ceilometer. Details on the radar calibration can be found in Tansey et al. [2022], and a complete listing of all the cloud and precipitation instruments deployed during MICRE can be found in McFarquhar et al. [2021].

The determination of cloud and precipitation boundaries begins by finding contiguous vertical regions (hereafter layers) of significant reflectivity (greater than the MDS) for each 12-second radar profile, with at least 100 m of clear sky (no significant reflectivity) between the layers. The ceilometer vendor's proprietary software appears to assign the cloud base at (or near) the peak in the measured backscatter, which in many cases will be slightly above the location where small cloud droplets can be found, i.e. the cloud base height (CBH). The ceilometer identifies CBH for up to 3 cloud layers (about once every 6 to 15 seconds, depending on the ceilometer). The ceilometer CBHs (regardless of which ceilometer observed it) are mapped onto the 12-second radar grid by aggregating all ceilometer CBHs within 30 seconds of each radar profile and assigning each CBH to the nearest radar layer, as long as the ceilometer CBH is no further than 100 m from the radar layer. (This 100 m allows for errors in the height determination, and for cases where the radar may be able to detect cloud top but not the less reflective region near cloud base). The result is a set of layers, each defined by a radar base height, a radar cloud top height, and a ceilometer cloud base height (taken as the median value of all the CBHs assigned to the layer). As will be discussed later, precipitation falling from low clouds is common place, and the radar layer base height is typically lower than the ceilometer CBH. Ceilometer CBHs which are more than 100 m from a known (radar) layer are taken to be part of an additional layer whose reflectivity is below the radar MDS, and its position is defined only by the median ceilometer CBH. This occurs about 10% of the time.

For the presented analysis, the above 12-second boundaries are further reduced onto a 5-minute grid, as described in this paragraph. A 5-minute grid is needed in part to obtain sufficient laser backscatter signal to estimate cloud base phase and the below-cloud precipitation phase; but this grid also substantially reduces the impact of noise in the radar boundaries and surface precipitation datasets. If at least one cloud layer is reported for at least one minute (at least 5 of the 25 12-second columns in each 5-minute period has a ceilometer CBH), we define the 5-minute analysis period as cloudy, and CBH is taken as the median CBH (i.e. the median when present). If the ceilometer reports more than one cloud base is present for at least one minute, we defined the cloud as multi-layered and the 5-minute median CBH is calculated for each layer. We likewise compute 5-minute median CTHs from the radar layer top heights (median when present).

The associated radiosonde temperature, and all phase retrievals, are based on the 5-minute median CTH & CBH pair from the cloud layer nearest to the surface, and “low clouds” specifically refers to clouds with a 5-minute median CTH < 3 km. As a sensitivity test, we re-calculated the cloud occurrence statistics (presented in section 3.1) but instead of using 1 minute (out of 5 minutes) as minimum requirement to identify cloud, we increased the threshold to 2 minutes. This causes the single-layer cloud occurrence frequency to increase by less than 3% at the expense of multi-layer occurrence, and total cloud occurrence did not change significantly (within the listed uncertainties).

To calculate cloud top temperature (CTT), twice-daily radiosonde launches at 00:00 UTC and 12:00 UTC are paired with radar/ceilometer cloud boundaries for the surrounding 12 hours of the launch. Some degree of uncertainty is expected in CTTs far from sonde launch times, as the vertical temperature profile may evolve over the course of the 12 hour period. To test the sensitivity of our results, statistics were re-calculated for the surrounding 6 hours of a launch, effectively halving the sample size. Results were within the estimated uncertainty ranges discussed below. Tightening the time range surrounding sonde launches did decrease the estimated retrieval error rate for cloud base thermodynamic phase (estimated using warm-topped clouds, discussed in the next section), but only by about 1%.

2.2 Depolarization Lidar

In addition to the laser ceilometers, the AAD deployed a 532 nm depolarization lidar. The lidar operated at 30 m vertical resolution, with further specifications given in Klekociuk et al. [2020] and Huang et al. [2015], and provided range-profiles of backscatter and depolarization ratio. We initially attempted to calibrate the AAD lidar following the method of O'Connor [2004], which relies on periods of fully attenuating, non-precipitating cloud. Unfortunately, we found the AAD calibration was not stable across the 7-month measurement period, sometimes changing significantly from one non-precipitating calibration period to the next. However, we found that we could calibrate the ceilometer using the O'Connor [2004] approach and that this calibration was stable over time. Therefore, in order to better calibrate the AAD system data, we developed an approach that scales the AAD polarization lidar backscatter to the stably-calibrated ceilometer backscatter for times that are far from periods where the O'Connor technique can be applied. Further details on this calibration transfer approach can be found in the Supporting Information, where we show that the transfer calibration factors compare well with calibration factors directly from the O'Connor method (during periods where such can be applied directly to the AAD lidar).

The AAD lidar also malfunctioned for 17 days during August and September, and these data are not included in the analysis. An artificial increase in the cross-polarization channel counts occurred from August-October, which we account for by scaling the depolarization ratios by a correction factor (see Supporting Information section S2). The AAD lidar was also pointed 4° off zenith to vastly reduce (but not quite eliminate) the effects of horizontally oriented ice crystals. The fractional occurrence of missing/bad data are given in section 3.2. We discuss the implications of the lidar data quality concerns in more detail in the concluding section.

2.3 Below-cloud precipitation

In Tansey et al. [2022], we give statistics of precipitation measured at the surface by blending data from the radar, disdrometer and tipping bucket for the first year of MICRE (April 2016 – April 2017). In this paper, we examine the thermodynamic phase of hydrometeors which were below-cloud base but evaporated/sublimated before reaching the surface. We specifically use the phrase "below-cloud" to mean the region 150 to 250 m below cloud base. Following MP18, frozen precipitating particles below cloud base polarize the returned backscatter and increase the measured depolarization ratio (δ_L), whereas scattering from spherical liquid drops has a small depolarization ratio. Unlike the situation in-cloud or at cloud base (section 2.4), multiple scattering has a minimal impact on the measured depolarization ratio below-cloud and can be neglected.

Based on an analysis of warm-topped clouds for which we know the precipitation must be liquid, we find 86% of these data have a $\delta_L \leq 0.05$, and only 7% have a $\delta_L > 0.1$. As we will discuss in section 2.4, seeder-feeder events can result in frozen/mixed phase particles below warm-topped clouds, and may be responsible for δ_L being larger than 0.05, and we have removed such events where we can. Nonetheless, it remains possible that seeding had occurred just prior to the cloud advecting over the radar, and is therefore still affecting the cloud though it is no longer obvious in the radar time-height data. Likewise, surface fog may result in multiple scattering that increases the below-cloud δ_L value and, again, we have removed cases containing surface fog to the degree that we can identify them from the ceilometer. Such events may nonetheless be responsible for some values of δ_L being larger than 0.05 some of the time. On the other hand, for events believed to have mixed or ice-phase precipitation at the surface (i.e. events where the surface disdrometer indicates that snow/mixed phase precipitation is present), the below-cloud δ_L is larger than 0.1 about 74% of the time, between 0.05 and 0.1 for 16% of the time, and less than 0.05 only 10% of the time. Accordingly, we ascribe below-cloud precipitation with δ_L less than 0.05 as liquid phase, between 0.05 and 0.1 as ambiguous or mixed phase, and greater than 0.1 as frozen. We stress that a depolarization ratio less than 0.05 does not guarantee that all particles are liquid, and some frozen or mixed phase particles may be present (but if so, they are not contributing substantially to the measured lidar backscatter), and vice-versa for depolarization ratios larger than 0.1.

As with all non-coaxial lidar systems, there is incomplete overlap between the AAD lidar's transmission beam and the field of view of the receiver at low altitudes. For this Macquarie Island campaign, we must restrict the analysis to altitudes of at least 250 m altitude above the surface; that is, phase is retrieved at cloud base and in below-cloud precipitation (100 to 200 m below CBH) restricted to CBH $\geq$ 450 m. In later sections, phase occurrence statistics are restricted to cases where the lowest cloud base is greater than 450 m from the surface. We report separately on macrophysical occurrence frequencies that include CBH < 450 m (Table #1).

2.4 Cloud Base Phase

The cloud base thermodynamic phase is retrieved following the approach described in Hu et al. [2007] and Mace et al. [2020]. As with the below-cloud retrieval, the cloud-base phase retrieval also relies on the lidar depolarization ratio (δ_L), but accounts for multiple scattering using the lidar measured layer-integrated attenuated backscatter (γ). Scattering due to spherical (liquid) particles is distinguished from scattering by horizontally-oriented ice crystals (HOI) based on the tendency of HOI to yield high γ and low δ_L. Similarly, randomly-oriented ice crystals (ROI) are identified based on their tendency to yield high δ_L values and low γ as depicted in Figure 1. Figure 1 shows data from warm clouds with CTT > 0°C. Boundaries initially proposed in Hu et al. [2007] to identify liquid phase particles (based on γ vs. δ_L) are plotted in cyan & green.

Points that lie above the cyan line are shown by Hu to be HOI, while points below the green line are ROI. Blue & red lines denote adjusted thresholds developed by Mace et al. [2020] for this same purpose. In this study, we use the thresholds defined by Hu to define HOI & ROI (that is, data points located below the green or above the cyan lines are considered HOI & ROI, respectively), and we consider those points located between the Mace & Hu lines to be mixed phase or ambiguous. Only those points between the red & blue Mace lines are considered likely to be liquid phase. As one expects, Figure 1 shows that the vast majority of the warm-topped clouds have a cloud base phase that is identified as liquid (95%).

Nominally, the Hu/Mace technique can only be applied when the lidar backscatter is fully attenuated by the cloud layer. Following O'Connor [2004], we define the lidar backscatter as fully attenuated if the backscatter drops by at least a factor of 20 from its in-cloud peak value within 300 m of the in-cloud peak. Otherwise, we define the lidar backscatter as either heavily attenuating if the backscatter drops by a factor 10 within 600 m of the peak, or lightly attenuating (if not fully or heavily attenuating). In the event that the lidar is only lightly attenuated for a 5-minute period, we still apply the retrieval technique limiting the layer to 300 m above cloud base. Most low clouds are found to be fully or heavily attenuating, and statistics on the relative occurrence of the cloud base phases (reported in section 3.2) do not change significantly if we exclude these lightly attenuating layers.

For the purpose of calculating the integrated backscatter, we define the start of the cloud layer as the region between CBH-100 m (just below the ceilometer defined base) and the first vertical point where the AAD lidar appears to be fully attenuated (no appreciable particulate scattering above this point), or as defined above for heavily and lightly attenuating clouds. We conservatively start at 100 m below ceilometer CBH because the vendor-retrieved cloud base tends to coincide with the peak in total backscatter, which is often somewhat above the altitude where small cloud-droplets can be found (and in which backscatter exponentially increases [O'Connor 2004]). The results do not change appreciably if we increase this level to CBH-50 m.

Upon visual inspection of individual cases, we found some events where a seeder-feeder mechanism is active in generating ice or mixed phase precipitation from what would otherwise be a warm cloud layer. Figure 2 shows one such case. Here cold clouds aloft are precipitating glaciated particles into the warm cloud layer near the surface, denoted by the red arrows. The radar Doppler velocity shows updrafts (negative velocities; purple coloration) near the top of the higher cloud, which is likely driving ice formation. The large downward Doppler velocity (in excess of 2.5 m/s), which is associated with the hydrometeors that have fallen from the upper layer and are now reaching the top of the low cloud (demarcated by the black dashed line), strongly suggests that the glaciated particles are melting. The nearest sonde puts the freezing level just above 1700 m. The surface disdrometer data likewise suggest that ice precipitation is present near the surface during (or around) the times that particles are observed to be falling into the low cloud. Our simple CTT screening cannot completely account for the presence of seeder-feeder events because the radar cannot detect all ice falling into the lower layer and can only show us what is happening when the cloud is above the radar. Where identified, seeder-feeder cases have been removed from the warm-cloud dataset used to estimate confidence in the phase retrievals. For the remaining warm-topped cloud cases, only about 5% of the data points in Figure 1 fall above/below the liquid phase boundaries.

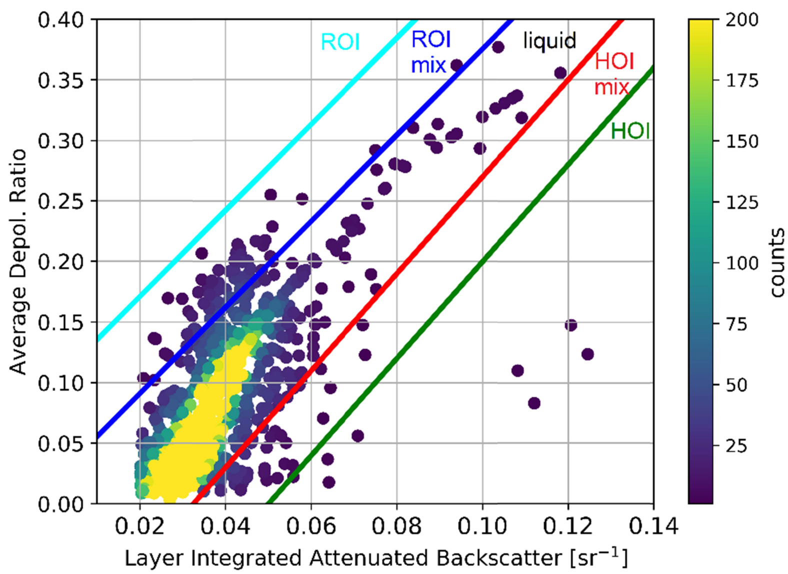

Figure 1: Cloud base layer γ vs. δ_L points for CTH < 3 km, CBH > 450 m and CTT > 0°C (i.e. this is for warm/liquid clouds). Lines/categories that identified HOI, ROI and liquid are as defined by Mace et al. [2020]; see text. The colorbar shows density of counts / number of 5-minute observations. Uncertainty is estimated to be about ±2.5% by considering the percentage of points above/below the liquid boundaries (blue and red lines).

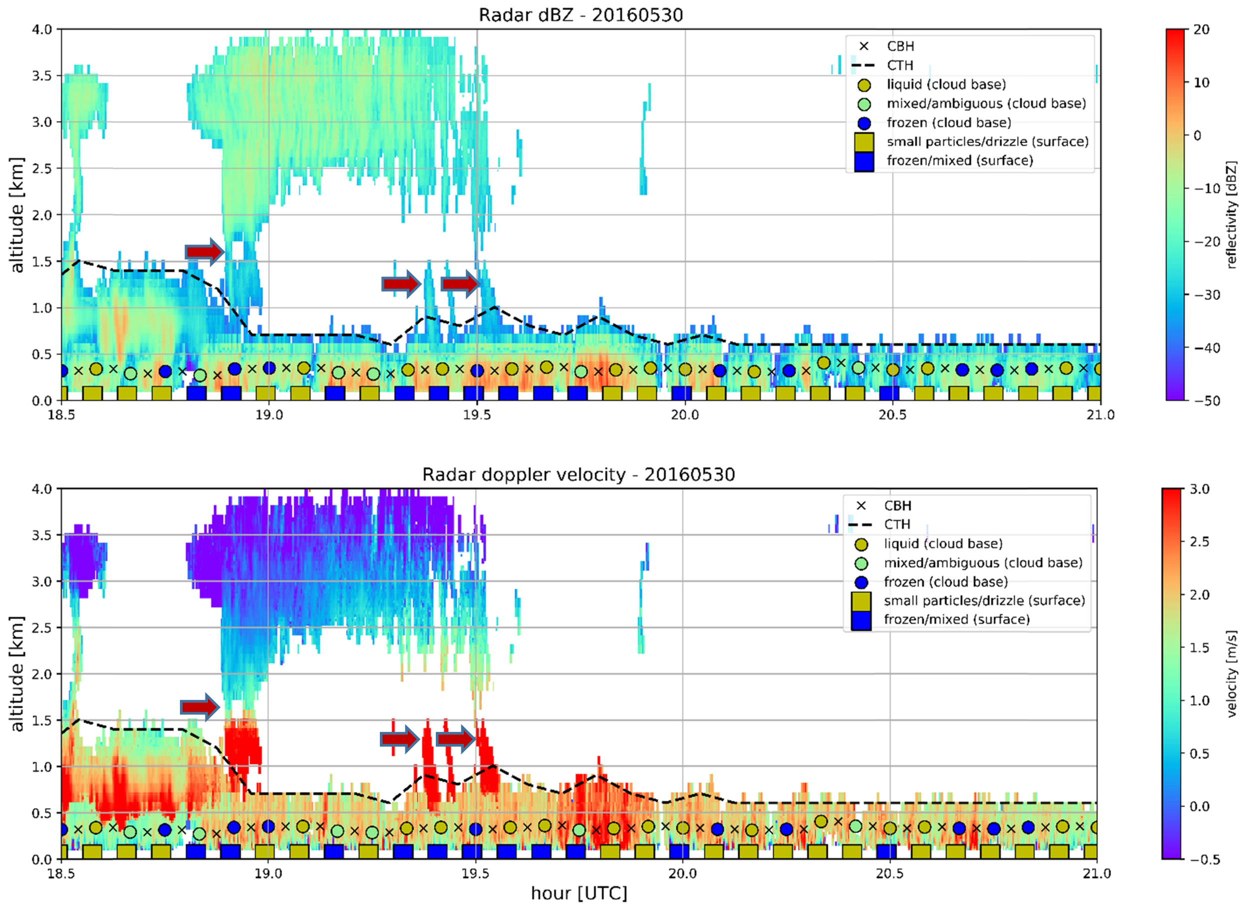

Figure 2: Example of a seeder-feeder event in which a higher cloud forms ice particles that seed precipitation in the lower cloud layer. Arrows overlaid on the plot point to obvious seeder-feeder instances. Cloud base height is marked by x's, cloud top height by dashed lines. The phase of particles at cloud base are given by dots (color-coded by phase). Precipitation phase at the surface (squares) are from the MICRE radar-disdrometer blended surface dataset [Tansey et al. 2022].

3. Results

This section presents results, starting with cloud macrophysical characteristics, specifically seasonal occurrence frequencies of single and multi-layer clouds below 3 km, for cold- and warm-topped clouds. Section 3.2 discusses the occurrence frequencies of various thermodynamic phases at cloud base. Section 3.3 gives occurrence frequencies of precipitation below warm- and cold-topped clouds as well as at the surface. Section 3.3 also examines below-cloud precipitation as a function of cloud base phase. Section 3.4 discusses the relationship between radar dBZ and lidar depolarization ratios in each season (April – November). Lastly, we present below-cloud precipitation depolarization ratios as a function of precipitating particle size (measured at the surface) in section 3.5.

3.1 Basic cloud macrophysics

The MICRE ceilometer, cloud radar and radiosonde datasets span a full annual cycle with only limited data gaps. We provide in Table #1 low cloud occurrence statistics for each season: austral summer (DJF), fall (MAM), winter (JJA) and spring (SON). All percentages are with respect to the number of good samples (that is, the number of 5 minute periods where radar and ceilometer data was collected within 12 hours of a successful sonde launch) in the time period specified. Results in sections 3.2 and 3.3 require polarization lidar, and thus only span April – November 2016, and occurrence statistics restricted to this period are also given at the bottom of the Table #1. Uncertainty ranges in all tables are the standard error, calculated as the standard deviation in the daily value divided by the square root of the number of days, treating each day as an independent sample. Estimating the uncertainty in this way provides the uncertainty in the mean for the MICRE period specified, but does not include interannual or other longer term variability. In short, one should not expect that cloud occurrence in another year will necessarily agree with that observed during the MICRE period within the Table #1 uncertainty ranges.

Percentages in the first two columns are seasonal occurrence frequencies of single and multi-layer clouds with tops below 3 km, respectively. The total of single and multilayer clouds is given in column 3. The data show that low clouds are common in all seasons, with summer (DJF) having only about 10% less cloud cover than winter (JJA). Columns 4 & 5 give the percentage of time that the lowest cloud layer is warm-topped vs. cold-topped. Percentages in columns 4 & 5 sum to the total in column 3. CTT refers to the lowest cloud top in the event that multiple layers are present. The data show that most low clouds had a CTT < 0°C. This is true in all seasons, with (not surprisingly) austral winter (JJA) having the highest absolute and relative occurrence of such cold cloud tops. In the annual average, a low cloud layer is present about 65% of the time with roughly 2/3 of this cloud having a CTT < 0°C.

The depolarization lidar based phase retrievals (discussed in the next three subsections) is limited to the subset of cases where cloud base is above 450 m. Column 6 gives the percentage of time that cloud top is below 3 km and cloud base is above 450 m, and this is further divided to the occurrence of low clouds with top temperatures > 0°C and ≤ 0°C in the final two columns.

These three columns are highlighted to emphasize that this is a separate and specific subset of low clouds used for lidar phase retrievals. The restriction is significant, with the occurrence of low clouds having a cloud base above 450 m being roughly 20 to 30% lower than the total occurrence of low clouds, depending on the time period. We will discuss the implications of this for interpreting the phase statistics in Section 4. Perhaps surprisingly, the difference is roughly equally split between warm- and cold-topped clouds in all seasons. For example, in winter (JJA) the occurrence of clouds with CBH > 450 m is about 30% lower than the occurrence of all clouds (that is, 39% of all good data points have low clouds with CBH > 450 m, as compared to 69% of all good data points having a low cloud with any CBH) with 13.6 % of the 30% being due to warm-topped clouds and the remaining 16.4% being due to cold-topped clouds.

Season	Single layer, CTH<3km, any CBH [%]	Multiple layers with CTH<3km, any CBH [%]	Total CTH<3km, any CBH [%]	CTH<3km, any CBH (lowest layer if multi-layered) and		CTH<3km, CBH>450m (lowest layer if multi-layered) [%]	CTH<3km, CBH>450m and	
				CTT>0°C [%]	CTT≤0°C [%]		CTT>0°C [%]	CTT≤0°C [%]
DJF	50.6±2.1	9.8±1.0	60.4±2.2	22.4±2.4	38.1±2.6	36.8±2.6	7.9±1.3	28.9±2.5
MAM	56.0±2.1	11.1±1.1	67.1±2.1	25.0±2.9	42.0±2.9	39.5±3.0	6.4±1.3	33.1±2.9
JJA	57.9±2.0	11.1±1.0	69.0±2.0	17.8±2.3	51.2±2.7	39.0±2.9	4.2±0.9	34.8±2.9
SON	54.0±2.2	10.2±0.9	64.2±2.4	17.9±2.3	46.3±2.9	44.6±3.1	6.8±1.2	37.8±3.1
MICRE (full year)	54.6±1.0	10.5±0.5	65.1±1.1	20.6±1.2	44.5±1.4	40.4±1.4	6.1±0.6	34.2±1.4
April-Nov.	56.1±1.3	10.5±0.6	66.6±1.3	19.4±1.5	47.2±1.7	40.8±1.8	5.3±0.6	35.5±1.8

Table 1: Low cloud occurrence characteristics. The first two columns show how frequently clouds with radar-lidar-derived tops below 3 km occur in single or multiple layers, respectively, with the total of columns 1 & 2 given in column 3. Columns 4 & 5 show warm/cold CTT percentages for the lowest cloud layer. E.g. DJF has single + multi-layer clouds ~60% of the time; warm-topped clouds 22% of the time + cold 38% = 60%. Column 6 shows the occurrence frequency of the subset of clouds used for phase retrievals (tops below 3 km and bases above 450 m). Columns 7 & 8 show warm/cold CTT percentages for the subset of low clouds with CBH > 450 m; i.e., CTT>0°C + CTT≤0°C in rows 7 & 8 will sum to the percentage in column 6.

Season	Warm-topped cloud mean			Cold-topped cloud mean		
	CBH [m]	CTH [m]	Thickness [m]	CBH [m]	CTH [m]	Thickness [m]
DJF	416±22	876±25	460±28	795±41	1674±41	879±56
MAM	360±25	893±40	532±45	737±39	1637±44	900±64
JJA	357±17	826±26	469±29	686±34	1543±41	857±50
SON	376±19	838±21	462±27	822±37	1631±37	809±47
MICRE (full year)	380±10	861±14	481±16	761±19	1620±21	859±27
April-Nov.	356±12	833±18	477±20	749±22	1595±25	847±31

Table 2: Mean boundaries and thicknesses by season for warm-topped (CTT>0°C) and cold-topped (CTT≤0°C) low clouds (CTH<3km). If multiple layers are present, the lowest cloud layer is used.

Table #2 gives mean cloud boundaries and thicknesses in each season, for the full year of MICRE, and for the April-November period. If multiple layers were present, boundaries for the lowest cloud layer are used in the averaging. Uncertainty in the mean values are again estimated by the standard error (standard deviation divided by the square root of the number of days). Warm clouds occur nearer to the surface (have a lower cloud base and cloud top) and are geometrical thinner on average than cold clouds. The cloud boundaries and thicknesses are fairly similar in all seasons, though arguably the clouds (both warm and cold topped) in winter are a bit closer to the surface than in summer and have lower CBHs and CTHs (with the difference just exceeding the sum of the estimated one-sigma uncertainties).

3.2 Cloud base phase statistics

The first three columns of Table #3 further subdivide the fractional occurrence of low clouds with CBH > 450 m into the fraction of time that the AAD depolarization lidar was fully or heavily attenuated by the low-cloud layer, followed by the fraction of time it was lightly attenuated, or the lidar data are missing or bad. (The sum of Table #3 columns 1-3 is equal to the percentage of time that there are cloud layers with CTH < 3 km and CBH > 450 m listed in Table #1, column 6). As discussed in section 2, we still retrieve a cloud base phase for lightly attenuating cloud layers by defining the cloud layer extending from CBH-100 m through CBH+300 m. Regarding bad data, in addition to the 17 days of bad data in August and September (mentioned at the end of Section 2.2) we also filter out a small number of individual data points with unphysical values that are significantly lower or higher than the range of integrated backscatters reported in Mace et al. [2020], e.g. $\gamma < 0.02$ sr^{-1} and $\gamma > 0.2$ sr^{-1}. These individual points comprise about 1.2% of data in AM, 0.7% of data in JJA and only 0.2% of data in SON. From August-October, the lidar performance (particularly the cross-polarization channel) degraded and required more meticulous correction; see Supporting Information.

As discussed in section 2 (see also Fig. 1) the cloud base phase of warm-topped clouds are overwhelmingly found to be liquid phase (95%), as one expects. For cold-topped clouds (CTT ≤ 0°C), the highlighted section of Table #3 (columns 4-6) gives the *relative* occurrence frequency of the cloud base phase such that liquid + HOI/mix + ROI/mix sum to 100% in each season. In qualitative agreement with previous studies (e.g. MP2018), we also find that the majority of cold-topped clouds are liquid phase at cloud base (86% in the April-Nov. period), and this is true in all months/seasons for which we have measurements. There is, arguably, a slightly greater occurrence of frozen and mixed/uncertain cloud base phase in fall (AM) and winter (JJA) compared to spring (SON). Removing the lightly attenuating clouds does not significantly change these relative occurrences.

Season	CTH<3km, CBH>450m, fully or heavily attenuated [%]	CTH<3km, CBH>450m, lightly attenuated (retrieval uses cloud base+300m) [%]	CTH<3km, CBH>450m, AAD lidar data missing/bad [%]	Liquid phase cloud base (CTT≤0°C clouds) [%]	Frozen or mixed HOI cloud base (CTT≤0°C clouds) [%]	Frozen or mixed ROI cloud base (CTT≤0°C clouds) [%]
AM	31.8±3.4	5.3±0.7	1.2±0.7	83.3±1.9	7.1±1.5	9.6±1.4
JJA	27.6±2.5	5.4±0.7	6.0±1.9	85.2±1.8	10.1±1.6	4.7±0.9
SON	31.7±2.8	8.3±1.0	4.6±1.7	88.2±1.8	8.6±1.7	3.2±0.7
April-Nov.	30.1±1.6	6.4±0.5	4.4±1.0	85.7±1.1	8.8±0.9	5.5±0.6

Table 3: Occurrence frequency (relative to all time) when low clouds are present with CBH>450 m and when depolarization lidar is (i) fully or heavily attenuated, (ii) not fully attenuated but still able to retrieve a cloud base phase, and (iii) missing or bad. The highlighted columns give the relative occurrence frequency of each cloud phase (these column sum to 100%) for times when CTT<0; for example, when cold-topped clouds are present and lidar data is good in April-May, 83.3% are liquid at cloud base, 7.1% HOI/mix and 9.6% ROI/mix, summing to 100%.

3.3 Precipitation just below cloud base

Table #4 contains seasonal occurrence frequencies of below-cloud precipitation, as well as the fraction of time that this precipitation reaches the surface (detected with the blended radar-disdrometer-tipping bucket dataset). The occurrence statistics in Table #4 are the relative percentages, meaning the fraction of good data when low clouds are present with CBH > 450 m and CTH < 3 km, and the condition listed in each column is met. For example, for the duration of the dataset (April-November) warm-topped low clouds only occur about 5% of the time (column 7, Table #1); when present, 72% of the time these warm-topped clouds are precipitating 150 to 250 m below the ceilometer cloud base. Overall, Table #4 shows that a significant majority (68% to 80%) of low clouds have precipitation falling from them, regardless of whether they are warm or cold-topped, and much of this precipitation does not reach the surface. The high occurrence of precipitation just below cloud base shown here – as well as the difference between below-cloud precipitation and precipitation at (or near) the surface – is consistent with Silber et al. [2021], who examine the prevalence of precipitation from supercooled clouds in the Antarctic, Stanford et al. [2023] who report similar below-cloud precipitation occurrence using the MICRE radar, and nearby ship campaigns like MP18. Most of this precipitation is comprised of small particles and has a precipitation rate below 0.5 mm/hour most of the time [Wang et al. 2015, Tansey et al. 2022].

Season	Warm low cloud precipitation [%]		Cold low cloud precipitation [%]	
	below-cloud	at surface	below-cloud	at surface
AM	72.1±4.6	41.3±5.8	72.9±4.2	42.2±4.4
JJA	78.8±3.4	47.0±4.4	79.8±2.1	51.3±3.4
SON	64.2±3.6	34.4±3.9	68.1±2.9	40.9±3.4
April-Nov.	71.4±2.2	40.6±2.6	74.0±1.7	45.3±2.1

*Table 4: Percentage relative to the subset of low cloud with CTH < 3 km, CBH > 450 m that have precipitation detected **(i)** in the layer extending from CBH-250 m to CBH-150 m and **(ii)** at the surface (using the radar-disdrometer-tipping bucket blended data product).*

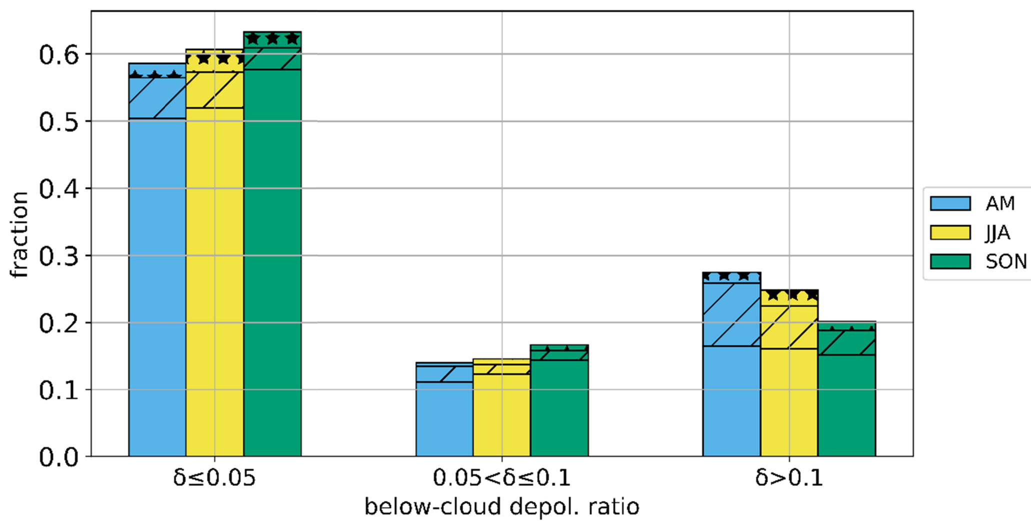

Figure 3: Fraction of below-cloud precipitation for clouds with CTT<0°C in each season by (i) cloud base phase (solid bars=liquid, dashes=mix/uncertain, stars=ice) and (ii) layer-averaged δ_L (horizontal axis).

In Fig. 3 we examine the relationship between cloud-base phase and below-cloud precipitation phase for cold-topped clouds. Precipitating clouds have been grouped by their below-cloud δ_L ranges, where δ_L < 0.5 means likely liquid phase precipitation and δ_L >0.1 means likely ice phase precipitation (that is, snow, graupel or ice pellets), as discussed in section 2. The hatching on each bar indicates the cloud base phase: solid means liquid, stripes are mixed/ambiguous and stars mean a pure ice phase cloud base (ROI or HOI crystals). Fractions in each season are relative to the number of successful phase retrievals; in other words, bars of each color (each season) sum to 1. In good agreement with MP18, we find that a significant fraction of low clouds are producing ice phase precipitation. MP18 find that 32% of precipitating low clouds (they used CTH < 4 km) with below-freezing cloud base temperatures were ice phase or producing ice phase precipitation (see their table #1). The data in our Fig. 3 is restricted to cold cloud tops (rather than cloud bases), nonetheless we similarly find 37 to 41% of cold clouds are producing ice or mixed/ambiguous phase precipitation (sum of last two columns), depending on the season. Unlike MP18, however, we also find that frozen precipitation is often falling from low clouds with liquid phase cloud bases. We will discuss this difference in more detail in Section 4.

3.4 Below-cloud precipitation phase by radar dBZ

In this section we build upon results presented in MP18 regarding the relationship between δ_L and radar reflectivity (dBZ) in below-cloud precipitation. Specifically, MP18 find that during the CAPRICORN experiment a W-band reflectivity in excess of -10 dBZ has δ_L values that are predominately larger than 0.05, indicative of ice-phase. This result has obvious practical value in terms of interpreting CloudSat and other radar observations, but also suggests that much (if not most) of the accumulated precipitation involves ice-phase microphysical processes (more on this in Section 4).

In Fig. 4 we present 2D joint histograms of lidar depolarization ratio and radar reflectivity associated with the below-cloud precipitation falling from cold-topped clouds (CTT ≤ 0°C) for three seasons (AM, JJA, SON). The color indicates the number of counts (of 5-minute periods) which fall into each histogram grid cell. We overlay lines at -10 dBZ and the three δ_L thresholds indicative of liquid, mixed/ambiguous, and ice phase to separate the histograms into six zones. The relative percentage of counts in each zone is also overlaid. Fig. 4 shows that for reflectivity factors below -10 dBZ, the precipitation is predominately liquid phase, and the occurrence of unambiguously ice phase precipitation ($\delta_L > 0.1$) greatly increases above the -10 dBZ line. Nonetheless, liquid phase particles ($\delta_L < 0.05$) are not rare above -10 dBZ. We examine the relative phase occurrence in more detail in Fig. 5.

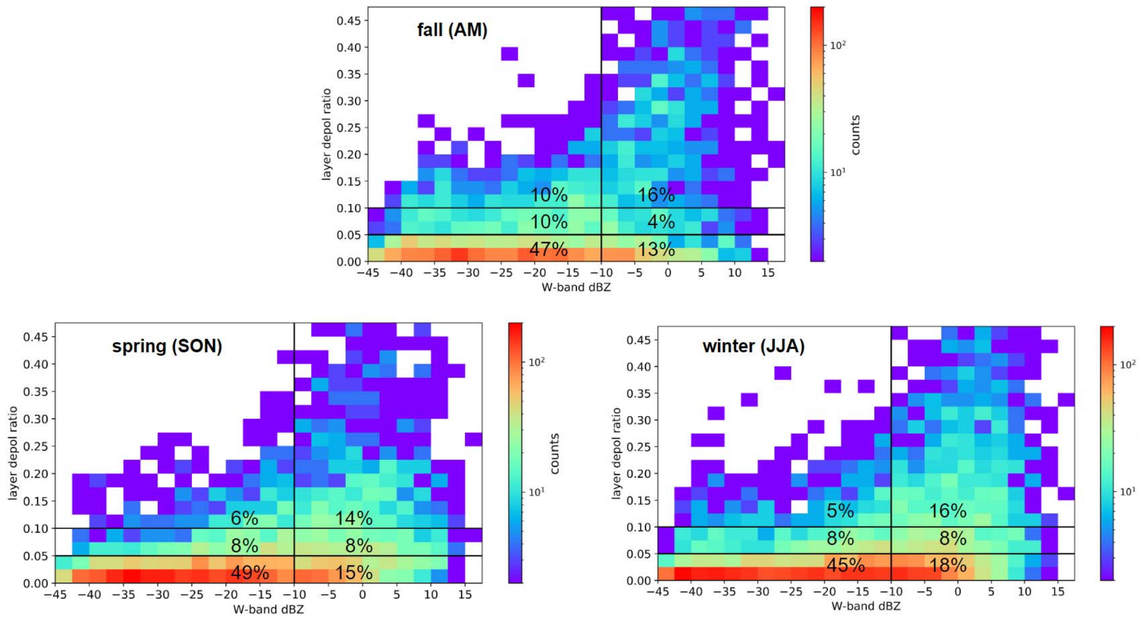

Figure 4: 2D histograms of δ_L vs. dBZ for precipitation below the bases of cold clouds, with the percentage of counts above/below -10 dBZ and in each δ_L phase regime.

In Fig. 5, we depict the relative occurrences of each phase category as a function of the reflectivity binned in steps of 2 dBZ, grouped by season. Normalization is done for each season such that for a particular season and reflectivity factor, the liquid, ambiguous and frozen fractional occurrence points sum to one. As inferred from Fig. 4, there is a significant increase in the relative occurrence of ice starting at about -10 dBZ. However, it is not until one reaches a reflectivity near 0 dBZ that ice is unambiguously more frequent than liquid phase precipitation.

Overall, the result in Figs. 4 and 5 confirm the finding from MP18, though they suggest the transition is more gradual. Possibly this difference is due to the short duration (a few weeks) of the dataset used by Mace and Protat. Remarkably, there appears to very little seasonal variation in this relationship. Taken at face value, the data in Fig. 5 suggest there is a greater tendency for ice phase precipitation in April and May, but given that the data still amount to (less than) a year of observations, this small difference may well not be significant.

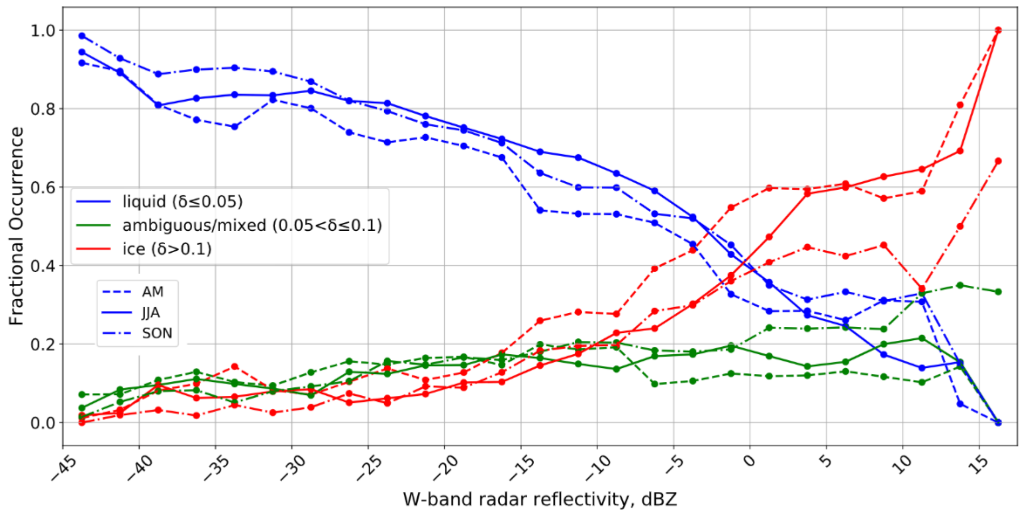

Figure 5: Fractional occurrence of liquid, ambiguous/mixed phase and ice at each reflectivity value. Phase-denominated points from a particular season sum to 1 in each reflectivity bin.

3.5 Below-cloud depolarization ratios and precipitation at the surface

In Fig. 6 we examine the relationship between the lidar below-cloud precipitation phase and the surface disdrometer (Parsivel2) derived particle type. Somewhat similar to Fig. 3, we plot the occurrence of surface precipitation in each below-cloud δ_L regimes (representing likely liquid, mixed/ambiguous, and likely ice) in each season. Here we include all clouds regardless of the CTT (though we hasten to add that most warm-topped clouds have a CBH too low for the below-cloud precipitation phase retrieval to be applied, and more than 80% of the clouds in this analysis have a CTT < 0°C). Precipitation reaching the surface at Macquarie Island is most often comprised of particles that are too small (diameters less than about 1 mm) for their type to be accurately determined by the surface Parsivel disdrometer, and Tansey et al. [2022] simply categorize these hydrometeors as “small particle precipitation”. The top panel in Fig. 6 shows the lidar depolarization ratios in the range 250 to 150 m below cloud base for particles categorized as “small” at the surface, while the bottom panel in Fig. 6 shows the below-cloud depolarization ratios when there are large particles at the surface. In the lower panel, stars denote large particles that are ice (frozen) or mixed phase at the surface. ~62% of small surface particles have a below-cloud phase that is likely liquid and ~22% likely ice, with the remainder being ambiguous, with little seasonal variability. Most large particles, on the other hand, are likely ice phase just below cloud base, with seasonal differences being more pronounced. SON has a lower fraction of below-cloud particles in the likely frozen category (58%) than AM & JJA (75% & 77%, respectively); instead SON has a larger fraction of mixed/ambiguous (27%) than AM & JJA (12% & 14%). In Tansey et al. [2022], our disdrometer analysis of precipitation at the surface also shows that SON contains more (large droplet) rain than MAM & JJA. Large particle precipitation includes essentially all surface precipitation with a precipitation rate above 0.5 mm/hr and is responsible for most of the total accumulated precipitation at Macquarie Island. The solid portion of the bars in this lower panel shows the fraction of large particle precipitation at the surface that is identified as rain. As the sizeable fraction of solid bar associated with below-cloud $\delta_L > 0.1$ (ice) demonstrates, ice (frozen) phase precipitation often melts before it reaches the surface and there is very little "warm rain" (rain that has formed without ice processes being involved) at Macquarie Island that is not small particle precipitation (that is, drizzle).

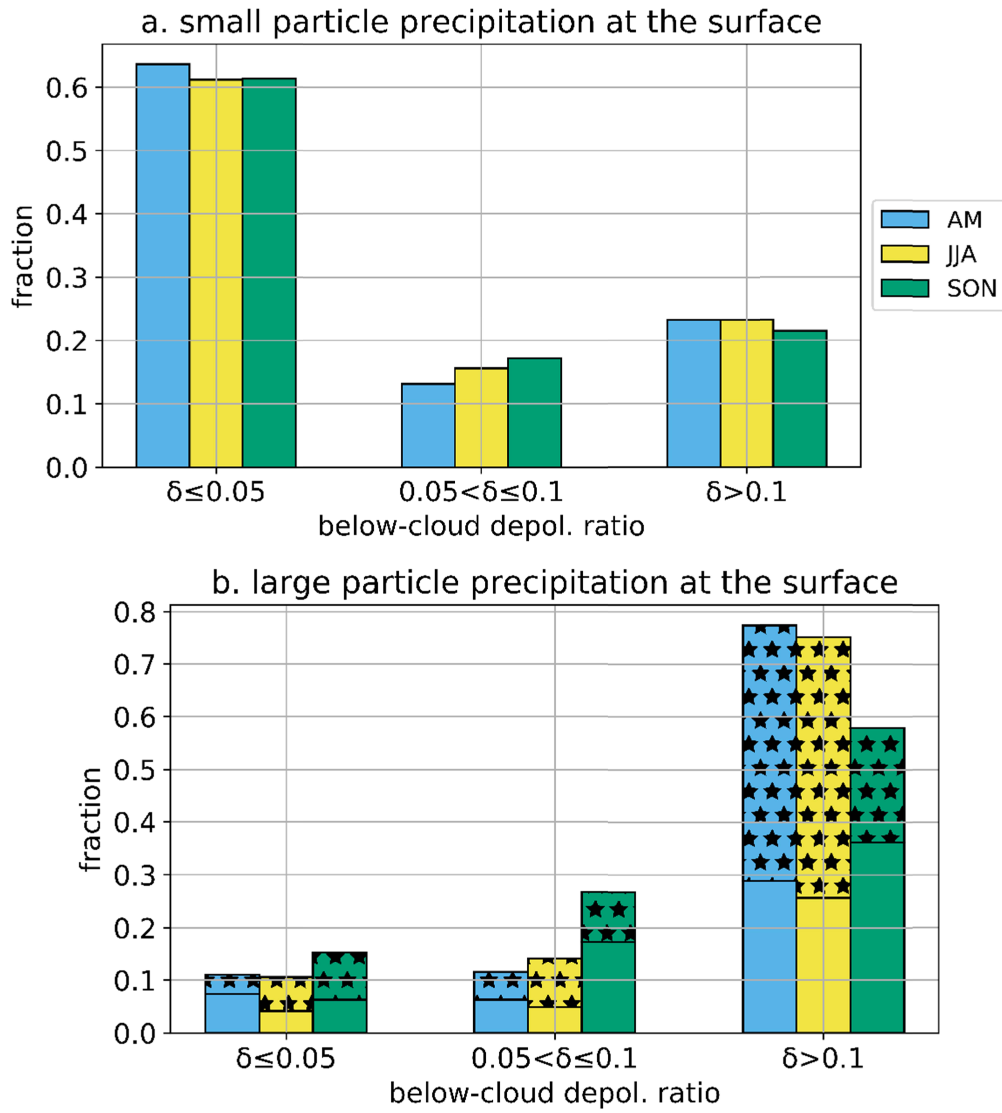

*Figure 6: **a.** Small-particle precipitation at the surface by season, split into different lidar δ_L phase regimes in the layer CBH-200 m through CBH-100 m. **b.** Same as **a.**, but for large particles. Precipitation for both warm- and cold-topped clouds is included. Solid colors represent rain, stars represent mixed/frozen as designated by the surface disdrometer. Phase specification is only possible for large particles (diameters > ~1 mm) with the Parsivel disdrometer.*

4. Discussion and Conclusions

Previous studies have examined the frequency of ice formation in SO low clouds from cloud top with satellite remote sensing, as well as from cloud base with radar and polarization lidar [Huang et al. 2015, Mace & Protat 2018, Mace et al. 2020, Mace et al. 2021a,b]. Satellites provide valuable insight into inter-annual and spatial variability of SO cloud properties, which the MICRE data cannot. Nonetheless, with the 7 consecutive months of depolarization lidar and almost 12 months of radar, ceilometer, surface disdrometer data collected during MICRE, we are able to build on these previous studies. We summarize below the main results in their order of presentation from sections 3.1 through 3.5, and discuss their implications.

1) During MICRE, low clouds occurred ~65% of the time (annually averaged), with DJF 2016-2017 having slightly less low cloud cover than JJA 2016. About ⅔ of low clouds are cold-topped (CTT < 0°C). On average, cold-topped low clouds are geometrically thicker and have cloud bases that are higher in altitude than warm-topped clouds, with only small seasonal differences.

Shipborne lidar-radar combined observations (MARCUS: Jan.-March 2018; CAPRICORN I: March-April 2016; CAPRICORN II: Jan.-Feb. 2018) in the vicinity of Macquarie Island (spanning latitudes 43°S to 68°S) have provided similar results. We find relatively similar cloud occurrence frequencies (Table #1) to those from the ship campaigns, even given the differences in location and criteria used to define low clouds. Protat et al [2017] report an absolute occurrence frequency of 77% for low clouds (1 week of data in March 2015) and MP18 report low clouds occur 65% of the time (March-April 2016), which matches the frequency we find during MICRE (ranging from 60-69% depending on the season). The seasonal differences across the MICRE year are small in both cloud occurrence frequencies and boundaries (base/top heights and geometric thicknesses; Table #2), although we find that CBH is higher on average in DJF & SON for both warm and cold clouds. While much of the concern regarding SO low clouds has focused on their shortwave impacts, as previously discussed by Hinkelman & Marchand [2020], cloud base height is important to the downward longwave flux, and downward longwave surface fluxes in the operational CERES SYN product are biased low in this region because satellite-estimated cloud bases used by CERES are too high and cold, especially at night.

2) Cloud base phase retrievals show that cold-topped low clouds are overwhelmingly liquid phase (~85%) in all seasons for which we have both depolarization lidar and radar measurements (April-Nov. 2016). During MICRE, there was a slightly greater occurrence of frozen and mixed/uncertain phase clouds in fall (AM) and winter (JJA) compared to spring (SON), but the difference is small (only a few percent). Given the potential for interannual variability, it would take several more years of data to establish whether or not this difference represents a true seasonal cycle.

Retrievals based on both satellite imagers (such as MODIS) and spaceborne lidar (CALIPSO) indicate the most SO cold-topped low clouds are predominantly liquid phase at cloud top [e.g., Huang et al. 2015]. Mace et al. [2021a] suggest that as little as 3% of the time, low clouds (CTH < 3 km) have ice-phase cloud tops based on CALIPSO measurements (this number includes both warm and cold topped clouds). We stress that having mostly liquid-phase cloud particles at either cloud top or cloud base does not mean that there is no ice in the cloud, or that ice phase processes are not active or important. As we discuss in more detail below, like MP18, we do find ice phase precipitation frequently falling from these supercooled liquid clouds.

Mace et al. [2021a] describe CALIPSO's tendency to identify clouds as liquid phase, even when ice is precipitating from them, as a failure or error of the satellite retrieval to identify the clouds as mixed phase. We do not dispute that the presence of precipitating ice must mean there are some small (cloud-droplet-sized) ice particles in the cloud. Nor do we dispute the Mace et al. [2021a] conclusion that the phase is identified to be liquid because visible photon scattering occurs predominantly in the upper portion of the cloud, whereas the ice is located deeper in the cloud. But for this same reason, we suggest that CALIPSO and imager retrievals (based on the scattering of visible photons) be referred to as "cloud top phase" retrievals, with no expectation that the retrieval will indicate whether or not ice is present deeper in the cloud. This is not entirely an issue of semantics. The identification of the cloud top phase as liquid (independent of ice precipitating from the bottom) has value in that it tells us something about the angular scattering dependence of the cloud, and how to convert measured shortwave radiances into shortwave fluxes. It also tells us that we can reasonably estimate cloud optical depth, liquid water path, and effective radius using visible-and-near-IR (MODIS-like [Nakajima & King 1990]) techniques that assume small spherical water droplets. In short, distinguishing cloud phase from precipitation phase is valuable in the same way as splitting the hydrometeor particle size distribution into separate cloud and precipitation components. An objective for retrievals should be to identify both the cloud and precipitation phases.

Regarding the cloud base phase, our results differ from MP18; MP18 suggest that cloud base phase is predominantly ice when ice-phase precipitation is falling from low clouds, and thus, they find that cloud bases are glaciated a larger fraction of the time than we find here (~29% vs. ~15% at most, since the 15% includes ambiguous cases). We speculate that this difference reflects a weakness in the cloud base phase retrieval used by MP18. The cloud base phase retrieval used in this article accounts for multiple scattering. This is not true of the approach used by MP18, which assumes that multiple scattering can be neglected in the first bin above cloud base. This is problematic because to the degree that the lidar backscatter is dominated by small cloud droplets, one expects that multiple scattering will be present and will increase the depolarization ratio; if scattering is not dominated by small cloud droplets, the contribution from any glaciated precipitation might also appreciably increase the depolarization ratio. In some larger sense, it is unlikely that clouds composed primarily of small frozen particles at cloud base would be composed primarily of small liquid particles at cloud top. Therefore, ice-phase cloud base occurrence should not substantially exceed ice-phase cloud top occurrence – and even our finding that ~85% of cloud bases are liquid should be treated as a lower bound for the occurrence of liquid phase clouds (i.e. clouds where most small cloud-size particles are liquid phase).

3) A significant majority of low clouds have precipitation falling from them regardless of CTT. Much of this precipitation does not reach the surface (Table #4).

The high occurrence of precipitation just below cloud base shown in Table #4, as well as the difference between below-cloud precipitation and precipitation at (or near) the surface, is consistent with Silber et al. [2021] examining the prevalence of precipitation from Antarctic supercooled clouds. It is also consistent with results presented by Stanford et al. [2023, submitted] for Macquarie Island based on the same W-band radar and ceilometer data used here, but processed independently. Stanford and co-authors provide a more in-depth analysis examining the dependence of precipitation on the radar sensitivity and distance from the cloud and surface. They also present a comparison of the observed data with GISS-ModelE3 simulations.

It is worth stressing that much of this light precipitation is too light for CloudSat to detect (in no small part because of surface clutter) or to identify as precipitation (rather than cloud) because the reflectivity is often < -15 dBZ, and the cloud base position is unknown, making it difficult to distinguish precipitation from cloud [Tansey et al. 2022, Stanford et al. 2023]. While these very light precipitation rates contribute only weakly to total accumulation at the surface, they have important implications for aerosol-cloud interactions and boundary layer thermodynamics. In particular, coalescence scavenging has been shown to be the primary sink of cloud condensation nuclei and has a large effect on cloud droplet number concentration, even at very low precipitation rates (e.g., 0.01 mm/hr) undetected by CloudSat [Kang et al. 2022]. This is true in both liquid and mixed phase precipitating clouds over the SO.

On a minor note, recent studies by Mace et al. [2021a,b] and MP18 report somewhat lower precipitation occurrence rates for SO low clouds based on W-band radar observations from the MARCUS and CAPRICORN ship cruises. In these studies, precipitation is identified when column or below-cloud maximum reflectivity is greater than -20 dBZ. In our study, we identify precipitation based on the presence of hydrometeors more than 150 m below the lidar ceilometer cloud base (regardless of reflectivity). We very often identify below-cloud precipitation with reflectivity factors below -20 dBZ, and therefore it is not surprising that these different criteria result in somewhat different occurrence statistics. We plan to explore this difference in future research focused on an analysis of MICRE-retrieved cloud and precipitation microphysical properties.

4) We observe that low clouds often produce ice phase precipitation, in agreement with MP18.

Similar to MP18, we find ~40% of cold-topped low clouds are producing ice or mixed/ambiguous phase precipitation. Ice/mixed phase cloud (and precipitation) occurrence is often episodic in nature. Lang et al. [2021] utilize a CAPRICORN case study to study ice/mixed phase – which alternates within patches of supercooled liquid – in open mesoscale cellular convective systems governed by shallow convection. They demonstrate a clear relationship between shallow convection and intermittently precipitating mixed phase clouds. Our extended time series from MICRE shows that 58% of mixed/frozen cloud bases persist for only a single 5-

minute period. A lower fraction of 40% persist 10 to 20 consecutive minutes; only 2% persist for a period longer than 20 minutes. These statistics substantiate the notion that frozen/mixed phase particles at cloud base generally exist within patches of supercooled liquid.

5) Also following MP18, we do find a significant increase in ice phase precipitation for below-cloud reflectivity factors in excess of -10 dBZ, but only above ~0 dBZ does ice surpass liquid as the predominant phase.

The relationship between reflectivity and phase is robust across the period examined (April - November 2016), and appears to be true during the summer as gauged from SOCRATES aircraft measurements [Kang et al. 2023, submitted]. Of course, part of the reason for this relationship is that radar reflectivity is a strong function of particle size and ice phase precipitation tends to form larger particles (see section 3.5), likely because of the Wegener–Bergeron–Findeisen process and efficient growth by accretion. Nonetheless, this suggests large reflectivity factors associated with cold-topped low clouds can be taken as indicative of ice-phase precipitation. If broadly representative of the SO, as seems likely, this result is very useful for the interpretation of satellite and aircraft radar data and the retrieval of precipitation rates.

6) Most drizzle (reflectivity < -10 dBZ, small-particle precipitation) is liquid phase directly below cloud base, while most large-particle precipitation is found to be ice phase.

As documented in our earlier study [Tansey et al. 2022], total accumulated surface precipitation is dominated by precipitation that contains large particles (particles with diameters > ~1 mm). The large-particle precipitation is classified as rain, ice pellets, wet snow or (dry) snow, based on the surface disdrometer retrieved particle size and velocity. Here we find that most of the large-particle precipitation identified by the disdrometer has a phase that is ice or mixed/ambiguous just below cloud base. This includes rain, meaning that most rain has formed from the melting of ice. The prevalence of ice precipitation underscores the importance of understanding and modeling both liquid and ice phase processes in SO low clouds. As Mülmenstädt et al. [2015] argue, this has important consequences for climate change.

In summary, the MICRE campaign has produced the longest timeseries of surface radar, ceilometer, and depolarization lidar observations to date over the SO. Uncertainty due to the lidar performance and calibration is a consideration for MICRE, particularly in August-October, during which time an abrupt step in the cross-polarization channel counts emerged. This was corrected by scaling depolarization ratios by a calibration factor determined using stable, well-calibrated periods earlier in the time series (see Supporting Information). Furthermore, the present data enable a 7-month-long analysis of cloud and precipitation phase. The combination of radar and depolarization lidar unfortunately does not extend to DJF, however, and consequently, we cannot estimate the degree to which summer low clouds produce less ice-phase precipitation. In an absolute sense, there will be less ice, simply because there is less cold-topped cloud. We speculate whether there is also a difference in ice amount driven by availability of aerosols that serve as primary INP (which appear to have a strong biological connection in data collected during the SH summer [Twohy et al. 2021]). Differences in boundary layer thermodynamics may also affect secondary ice processes. While the SOCRATES aircraft observations have added substantially to existing in situ data for the SO, there remains a strong need for more in situ data, especially measurements during the winter and data for use in process modeling studies. This is not to discount the value of collecting additional surface data from Macquarie Island. There does appear to be a modest level of variability (~5%-10%) from April to November. But given the potential for interannual variability, it will take several more years of data to be confident that this is the climatological norm. Additional data would also be very useful in estimating cloud feedbacks, for example, following the approach in Terai et al. [2019] applied to measurements at several Northern Hemisphere ARM sites.

Data availability

Data collected during MICRE are available via the ARM data archive (https://adc.arm.gov/). The radar-lidar cloud base and below-cloud precipitation retrievals, as well as 5-minute reduced radar and lidar time series, are available at [*submitted to the ARM archive, DOI's pending*].

Acknowledgments

This work was supported by the U.S. Department of Energy Atmospheric System Research program through Grant DE-SC0016225 and NASA through Grant NNX16AM05G. Technical and logistical support for the deployment to Macquarie Island were provided by the Australian

Antarctic Division through Australian Antarctic Science Project 4292, and we thank George Brettingham-Moore, Ken Barrett, Nick Cartwright, Nick Cole (deceased), Emry Crocker, Terry Egan, John French, Eric King (deceased), Ian McRobert, Lloyd Symons, Peter de Vries and Steven Whiteside for all of their assistance. We would also like to thank Adrian McDonald for providing the University of Canterbury ceilometer data used to supplement the ARM ceilometer.

References

- Bodas-Salcedo, A., P.G. Hill, K. Furtado, K.D. Williams, P.R. Field, J.C. Manners, P. Hyder, Kato, S. (2016). Large Contribution of Supercooled Liquid Clouds to the Solar Radiation Budget of the Southern Ocean. *J. Climate, 29*, 4213-4228, https://doi.org/10.1175/JCLI-D-15-0564.1
- Ceppi, P., Y.-T. Hwang, D. M. W. Frierson, and D. L. Hartmann (2012). Southern Hemisphere jet latitude biases in CMIP5 models linked to shortwave cloud forcing. *Geophys. Res. Lett., 39*, L19708, doi:10.1029/2012GL053115.
- Ceppi, P., Y.-T. Hwang, X. Liu, D. M. W. Frierson, and D. L. Hartmann (2013). The Relationship Between the ITCZ and the Southern Hemispheric Eddy-Driven Jet, *J. Geophys. Res. Atmos.*, *118*, 5136–5146, doi:10.1002/jgrd.50461
- Ceppi, P., Hartmann, D., Webb, M. (2015). Mechanisms of the Negative Shortwave Cloud Feedback in Middle to High Latitudes, *Journal of Climate, 29,* 139-157. DOI: 10.1175/JCLI-D-15-0327.1
- Cesana, G. V., Khadir, T., Chepfer, H., & Chiriaco, M. (2022). Southern ocean solar reflection biases in CMIP6 models linked to cloud phase and vertical structure representations. Geophysical Research Letters, 49, e2022GL099777. https://doi.org/10.1029/2022GL099777
- Delanoë, J., A. Protat, J.-P. Vinson, W. Brett, C. Caudoux, F. Bertrand, J. Parent du Chatelet, R. Hallali, L. Barthes, M. Haeffelin, and Dupont, J.-C. (2016). BASTA, a 95 GHz FMCW Doppler radar for cloud and fog studies. *J. Atmos. Oceanic Tech., 33*, 1023-1038, https://doi.org/10.1029/95JD03068
- DeMott, P. J., Hill, T. C. J., McCluskey, C. S., Prather, K. A., Collins, D. B., Sullivan, R. C., Ruppel, M. J., Mason, R. H., Irish, V. E., Lee, T., Hwang, C. Y., Rhee, T. S., Snider, J. R., McMeeking, G. R., Dhaniyala, S., Lewis, E. R., Wentzell, J. J. B., Abbatt, J., Lee, C., Sultana, C. M., Ault, A. P., Axson, J. L., Diaz Martinez, M., Venero, I., Santos-Figueroa, G., Stokes, M. D., Deane, G. B., Mayol-Bracero, O. L., Grassian, V. H., Bertram, T. H., Bertram, A. K., Moffett, B. F., and Franc, G. D. (2016). Sea spray aerosol as a unique source of ice nucleating particles, *P. Natl. Acad. Sci. USA, 113*, 5797–5803, https://doi.org/10.1073/pnas.1514034112
- Fan, J., Ghan, S., Ovchinnikov, M., Liu, X., Rasch, P. J., and Korolev, A. (2011). Representation of Arctic mixed-phase clouds and the Wegener-Bergeron-Findeisen process in climate models: Perspectives from a cloud-resolving study, J. Geophys. Res., 116, D00T07, doi:10.1029/2010JD015375.
- Frey, W. & Kay, J. (2018). The influence of extratropical cloud phase and amount feedbacks on climate sensitivity *Clim. Dyn.* 50:3097–3116 DOI 10.1007/s00382-017-3796-5

- Gettelman, A., Hannay, C., Bacmeister, J. T., Neale, R. B., Pendergrass, A. G., Danabasoglu, G., et al. (2019). High climate sensitivity in the Community Earth System Model Version 2 (CESM2). *Geophysical Research Letters, 46*, 8329–8337. https://doi.org/10.1029/2019GL083978
- Hinkelman, L. M., Marchand, R. (2020). Evaluation of CERES and CloudSat surface radiative fluxes over Macquarie Island, the Southern Ocean. Earth and Space Science, 7, e2020EA001224. https://doi.org/10.1029/2020EA001224
- Hu, Y., Vaughn, M., MCClain, C., Behrenfeld, M., Maring, H., Anderson, D., et al., (2007). Global statistics of liquid water content and effective number concentration of water clouds over ocean derived from combined CALIPSO and MODIS measurements. *Atmospheric Chemistry and Physics, 7*(12), 3353–3359. https://doi.org/10.5194/acp-7-3353-2007
- Huang, Y., A. Protat, S. T. Siems, and M. J. Manton, 2015: A-Train observations of maritime mid-latitude storm-track cloud systems: Comparing the Southern Ocean against the North Atlantic. J. Climate, 28, 1920–1939, doi:10.1175/JCLI-D-14-00169.1.
- Huang Y, Siems ST, Manton MJ, Rosenfeld D, Marchand R, McFarquhar GM, Protat A. (2016), What is the role of sea surface temperature in modulating cloud and precipitation properties over the Southern Ocean? *J. Clim. 29*: 7453–7476. https://doi.org/10.1175/JCLI-D-15-0768.1.
- Huang, Y., Franklin, C.N., Siems, S.T., Manton, M.J., Chubb, T., Lock, A., Alexander, S., Klekociuk, A. (2015). Evaluation of boundary-layer cloud forecasts over the Southern Ocean in a limited-area numerical weather prediction system using in situ, space-borne and ground-based observations. *Q. J. R. Meteorol. Soc.*, *141*, 2259–2276. DOI:10.1002/qj.2519
- Hwang, Y. & Frierson, D. (2013). Link between the double-Intertropical Convergence Zone problem and cloud bias over Southern Ocean. *Proceedings of the National Academy of Sciences of the United States of America. 110*, doi:10.1073/pnas.1213302110.
- Kang, L., Marchand, R. T., Wood, R., & McCoy, I. L. (2022). Coalescence scavenging drives droplet number concentration in Southern Ocean low clouds. *Geophysical Research Letters, 49*, e2022GL097819. https://doi. org/10.1029/2022GL097819
- Kay, J.E., C. Wall, V. Yettella, B. Medeiros, C. Hannay, P. Caldwell, C. Bitz. (2016). Global Climate Impacts of Fixing the Southern Ocean Shortwave Radiation Bias in the Community Earth System Model (CESM). *J. Climate, 29*, 4617-4636, https://doi.org/10.1175/JCLI-D-15-0358.1
- Kollias, P., and Albrecht, B. (2005). Why the melting layer radar reflectivity is not bright at 94 GHz, *Geophys. Res. Lett., 32*, L24818, doi:10.1029/2005GL024074.
- Kuma, P., McDonald, A. J., Morgenstern, O., Alexander, S. P., Cassano, J. J., Garrett, S., Halla, J., Hartery, S., Harvey, M. J., Parsons, S., Plank, G., Varma, V., and Williams, J. (2020). Evaluation of Southern Ocean cloud in the HadGEM3 general circulation model and MERRA-2 reanalysis using ship-based observations, Atmos. Chem. Phys., 20, 6607–6630, https://doi.org/10.5194/acp-20-6607-2020
- Lang, F., Huang, Y., Protat, A., Truong, S. C. H., Siems, S. T., & Manton, M. J. (2021). Shallow convection and precipitation over the Southern Ocean: A case study during the CAPRICORN 2016 field campaign. Journal of Geophysical Research: Atmospheres, 126, e2020JD034088. https://doi.org/10.1029/2020JD034088
- Lauer, A., Bock, L., Hassler, B., Schröder, M., & Stengel, M. (2023). Cloud Climatologies from Global Climate Models—A Comparison of CMIP5 and CMIP6 Models with Satellite Data, Journal of Climate, 36(2), 281-311, DOI: 10.1175/JCLI-D-22-0181.1

- Löffler-Mang, M., J. Joss (2000). An Optical Disdrometer for Measuring Size and Velocity of Hydrometeors. *J. Atmos. Oceanic Technol., 17*(2), 130-139, https://doi.org/10.1175/1520-0426(2000)017<0130:AODFMS>2.0.CO;2
- Mace, G. G. (2010). Cloud properties and radiative forcing over the maritime storm tracks of the Southern Ocean and North Atlantic derived from A-Train, *J. Geophys. Res.*, 115, D10201, doi:10.1029/2009JD012517.
- Mace, G.G., and A. Protat. (2018) Clouds over the Southern Ocean as observed from the R/V Investigator during CAPRICORN: Part I: Cloud occurrence and phase partitioning, *J. Appl. Meteor. Clim., 57*, 1783-1804. doi:10.1175/JAMC-D-17-0194.1.
- Mace, G. G., Benson, S., & Hu, Y. (2020). On the frequency of occurrence of the ice phase in supercooled Southern Ocean low clouds derived from CALIPSO and CloudSat. Geophysical Research Letters, 47, e2020GL087554. https://doi.org/10.1029/2020GL087554
- Mace, G. G., Protat, A., & Benson, S. (2021a). Mixed-phase clouds over the Southern Ocean as observed from satellite and surface based lidar and radar. *Journal of Geophysical Research: Atmospheres*, *126*, e2021JD034569. https://doi.org/10.1029/2021JD034569
- Mace, G. G., Protat, A., Humphries, R. S., Alexander, S. P., McRobert, I. M., Ward, J., et al. (2021b). Southern Ocean cloud properties derived from CAPRICORN and MARCUS data. *Journal of Geophysical Research: Atmospheres, 126*, e2020JD033368. https://doi.org/10.1029/2020JD033368
- Mallet, M. D., Humphries, R.S., Fiddes, S. L., Alexander, S. P., Altieri, K., Angot, H., Anilkumar, N., Bartels-Rausch, T., Creamean, J., Dall'Osto, M., Dommergue, A., Frey, M., Henning, S., Lannuzel, D., Lapere, R., Mace, G. G., Mahajan, A. S., McFarquhar, G. M., Meiners, K. M., Peeken, I., Protat, A., Schmale, J., Steiner, N., Sellegri, K., Thomas, J. L., Willis, M. D., Winton, V. H. L., Woodhouse, M. T., Miljevic, B., Simo, R., (2023). Untangling the influence of Antarctic and Southern Ocean life on clouds. *Elementa Science of the Anthropocene*, **11**, 1, doi:10.1525/elementa.2022.00130
- McCluskey, C. S., Hill, T. C. J., Humphries, R. S., Rauker, A. M., Moreau, S., Strutton, P. G., et al. (2018). Observations of ice nucleating particles over Southern Ocean waters. *Geophysical Research Letters, 45*(11), 989–997. https://doi.org/10.1029/2018GL079981
- McCoy, I. L., McCoy, D. T., Wood, R., Regayre, L., Watson-Parris, D., Grosvenor, D. P., Mulcahy, J. P., Hu, Y., Bender, F. A.- M., Field, P. R., Carslaw, K. S., and Gordon, H. (2020). The Hemispheric Contrast in Cloud Microphysical Properties Constrains Aerosol Forcing*, P. Natl. Acad. Sci. USA, 117*, 18998–19006, https://doi.org/10.1073/pnas.1922502117
- McFarquhar, G. M., Bretherton, C. S., Marchand, R., Protat, A., DeMott, P. J., Alexander, S. P., Roberts, G. C., Twohy, C. H., Toohey, D., Siems, S., Huang, Y., Wood, R., Rauber, R. M., Lasher-Trapp, S., Jensen, J., Stith, J. L., Mace, J., Um, J., Järvinen, E., Schnaiter, M., Gettelman, A., Sanchez, K. J., McCluskey, C. S., Russell, L. M., McCoy, I. L., Atlas, R. L., Bardeen, C. G., Moore, K. A., Hill, T. C. J., Humphries, R. S., Keywood, M. D., Ristovski, Z., Cravigan, L., Schofield, R., Fairall, C., Mallet, M. D., Kreidenweis, S. M., Rainwater, B., D'Alessandro, J., Wang, Y., Wu, W., Saliba, G., Levin, E. J. T., Ding, S., Lang, F., Truong, S. C. H., Wolff, C., Haggerty, J., Harvey, M. J., Klekociuk, A. R., & McDonald, A. (2021). Observations of Clouds, Aerosols, Precipitation, and Surface Radiation over the Southern Ocean: An Overview of CAPRICORN, MARCUS, MICRE, and SOCRATES, *Bulletin of the American Meteorological Society, 102*(4), E894-E928. Retrieved Dec 5, 2022, from https://journals.ametsoc.org/view/journals/bams/102/4/BAMS-D-20-0132.1.xml

- Mülmenstädt, J., O. Sourdeval, J. Delanoë, and J. Quaas (2015). Frequency of occurrence of rain from liquid-, mixed-, and ice-phase clouds derived from A-Train satellite retrievals, Geophys. Res. Lett., 42, 6502–6509, doi:10.1002/2015GL064604.
- Nakajima, T., & King, M. D., (1990). Determination of the Optical Thickness and Effective Particle Radius of Clouds from Reflected Solar Radiation Measurements. Part I: Theory. J. Atmos. Sci., 47, 1878–1893, https://doi.org/10.1175/1520-0469(1990)047<1878:DOTOTA>2.0.CO;2
- O'Connor, E. J., Illingworth, A. J., & Hogan, R. J., (2004). A technique for autocalibration of cloud lidar. *Journal of Atmospheric and Oceanic Technology, 21*(5), 777–786. https://doi.org/10.1175/1520-0426(2004)021%3C0777:ATFAOC%3E2.0.CO;2
- Protat, A., Schulz, E., Rikus, L., Sun, Z., Y. Xiao, Y. and Keywood, M. (2017) Shipborne observations of the radiative effect of Southern Ocean clouds, *J. Geophys. Res. Atmos., 122*, 318–328, doi:10.1002/2016JD026061.
- Sallée, J.-B., Shuckburgh, E., Bruneau, N., Meijers, A. J. S., Bracegirdle, T. J., Wang, Z., and Roy, T. (2013). Assessment of Southern Ocean water mass circulation and characteristics in CMIP5, models: Historical bias and forcing response, *J. Geophys. Res. Oceans*, *118*, 1830– 1844 doi:10.1002/jgrc.20135.
- Schuddeboom, A. J., & McDonald, A. J. (2021). The Southern Ocean radiative bias, cloud compensating errors, and equilibrium climate sensitivity in CMIP6 models. *Journal of Geophysical Research: Atmospheres*, 126, e2021JD035310. https://doi.org/10.1029/2021JD035310
- Schneider, D. P., & Reusch, D. B. (2016). Antarctic and Southern Ocean Surface Temperatures in CMIP5 Models in the Context of the Surface Energy Budget, Journal of Climate, 29(5), 1689-1716. https://doi.org/10.1175/JCLI-D-15-0429.1
- Silber, I., Fridlind, A. M., Verlinde, J., Ackerman, A. S., Cesana, G. V., and Knopf, D. A. (2021). The prevalence of precipitation from polar supercooled clouds, Atmos. Chem. Phys., 21, 3949–3971, https://doi.org/10.5194/acp-21-3949-2021
- Tansey, E., Marchand, R., Protat, A., Alexander, S. P., & Ding, S. (2022). Southern Ocean precipitation characteristics observed from CloudSat and ground instrumentation during the Macquarie Island Cloud & Radiation Experiment (MICRE): April 2016 to March 2017. *Journal of Geophysical Research: Atmospheres, 127*(5). https://doi.org/10.1029/2021JD035370
- Terai, C. R., Zhang, Y., Klein, S. A., Zelinka, M. D., Chiu, J. C., & Min, Q. (2019). Mechanisms behind the extratropical stratiform low-cloud optical depth response to temperature in ARM site observations. Journal of Geophysical Research: Atmospheres, 124, 2127–2147. https://doi.org/10.1029/2018JD029359
- Tokay, A., Petersen, W. A., Gatlin, P., and Wingo, M. (2013), Comparison of Raindrop Size Distribution Measurements by Collocated Disdrometers, *Journal of Atmospheric and Oceanic Technology*, *30*(8), 1672-1690, https://doi.org/10.1175/JTECH-D-12-00163.1
- Twohy, C. H., DeMott, P. J., Russell, L. M., Toohey, D. W., Rainwater, B., Geiss, R., et al. (2021). Cloud-nucleating particles over the Southern Ocean in a changing climate. Earth's Future, 9, e2020EF001673. https://doi.org/10.1029/2020EF001673
- Trenberth, K. and J. Fasullo. (2010), Simulation of present-day and twenty-first century energy budgets over the Southern Ocean, *J. Climate, 23*, 440-454, doi: 0.1175/2009JCLI3152.1

- Wang, Z., S. Siems, D. Belusic, M. Manton, and Y. Huang. (2015), A climatology of the precipitation over the Southern Ocean as observed at Macquarie Island. *J. Appl. Meteorol. Climatol., 54*, 2321-2337, doi:10.1002/grl.50986
- Williams, K.D., Webb, M.J. (2009), A quantitative performance assessment of cloud regimes in climate models. Clim Dyn (2009) 33:141–157, doi: 10.1007/s00382-008-0443-1
- Wood, R. (2012), Stratocumulus Clouds, *Monthly Weather Review*, *140*(8), 2373-2423., doi: 10.1175/MWR-D-11-00121.1
- Zelinka, M. D., Myers, T. A., McCoy, D. T., Po-Chedley, S., Caldwell, P. M., Ceppi, P., et al. (2020), Causes of higher climate sensitivity inCMIP6 models. *Geophysical Research Letters, 47*, e2019GL085782. https://doi.org/10.1029/2019GL085782

Supporting Information References

- Hu, Y., Liu, Z., Winker, D., Vaughan, M., Noel, V., Bissonnette, L., Roy, G., and McGill, M. (2006) Simple relation between lidar multiple scattering and depolarization for water clouds, *Opt. Lett. 31*, 1809-1811

Journal of Geophysical Research – Atmospheres

Supporting Information for

Southern Ocean low cloud and precipitation phase observed during the Macquarie Island Cloud and Radiation Experiment (MICRE)

Emily Tansey[1], Roger Marchand[1], Simon P. Alexander[2,3], Andrew R. Klekociuk[2,3], and Alain Protat[2,4]

[1]University of Washington, Seattle, Washington, United States

[2]Australian Antarctic Division, Hobart, TAS, Australia

[3]Australian Antarctic Partnership Program, Institute for Marine and Antarctic Studies, University of Tasmania, Hobart, TAS, Australia

[4]Australian Bureau of Meteorology, Melbourne, Victoria, Australia

Contents of this file

Text S1 to S2

Figures S1 to S3

Introduction

This document details in section S1 the calibration of the Australian Antarctic Division (AAD) lidar following O'Connor [2004], as well as a novel approach that scales the lidar backscatter to match that of the ceilometer in periods containing light below-cloud precipitation when the O'Connor method cannot be used. Section S2 describes an additional calibration of depolarization ratios from August-October, wherein we scale depolarization ratios from August-October by a constant factor calculated from liquid precipitation during the well-calibrated period prior.

S1. Polarization lidar backscatter calibration

We rely on both depolarization ratios and lidar backscatter measurements from the AAD polarization lidar (532 nm) obtained from April 6 to November 20 2016. Several sources of potential instability over the course of the time series were noted, namely three flashlamp changes (April 5, June 6 and Oct. 4) and an earthquake on Sept 8. In any case, we do not observe any notable increases in variability or performance degradation directly on or following these dates. Rather the lidar calibration is generally unstable throughout the 7 months (see Fig. S1). This instability is readily observable in the magnitude of the total (particulate + molecular) attenuated backscatter, and we therefore developed a time series of calibration scaling factors, as described below.

Initial calibration was based on measured photon counts in the height range 10 to 15 km, obtained during a clear-sky period on May 22, and matching the observed cross- and co-polar backscatter to that expected from molecular scattering. The near-surface aerosol optical depth was taken to be 0.05. The calibration is normalized with respect to laser output power and assumes an overlap correction. In spite of the overlap correction, there is an artifact (a narrow range with increased depolarization and total backscatter) near 250 m. This may or may not be indicative of some bias in the overlap correction, at least near the surface. Regardless, in this study we only used the data beyond 250 m to avoid this artifact.

We find that the total backscatter field in particular requires additional calibration. Starting with 5-minute backscatter, we apply the approach detailed in [O'Connor 2004]. This method requires cloud layers to be dense, liquid, optically thick, fully attenuating and non-precipitating, and thus nominally can only be applied to a small fraction of SO low clouds. O'Connor [2004] identified fully attenuated cloud layers as those that reduce the total backscatter by at least a factor of 20 from its in-cloud peak value within 300 m of the in-cloud peak. As noted in the main text of this paper, we loosen the criteria to include "heavily attenuating" clouds (backscatter drops by a factor of 10 within 600 m of the peak). Nonetheless, the total number of periods suitable to apply the calibration remains limited. The time series of calibration coefficients is shown in Fig. S1. Here the time series has been subject to additional noise filtering as shown in the flow chart in Fig. S2. Specifically, an O'Connor estimated calibration coefficient is initially determined on a 5-minute time scale (where the cloud is present for at least 1 minute). At the 5-minute scale, the cloud must be heavily or fully attenuating (as defined above). We do include precipitating clouds, and found that this made little difference in the overall calibrations. A 5-day running median (median of coefficients from that day and the surrounding ±2 days) is then taken.

Estimated values for the calibration coefficients that are more than factor of 2 from the 5-day median ($k_{5day}/2 < k$ or $k > 2\times k_{5day}$) are replaced by the median value. The resulting timeseries of calibration factors in shown by the blue line in Fig. S1.

In order to increase confidence in the calibration, we also calibrated the AAD lidar against the ARM ceilometer, whose calibration is stable (i.e. it appears to be constant in time when using the O'Connor technique). Specifically, we exploit the fact that for light (below-cloud) precipitation, one expects the total backscatter from the ceilometer and the AAD lidar to be the same. Here light precipitation means the contribution of multiple-scattering is small. We determine a transfer calibration coefficient (k_{tr}) by calculating the scale factor needed to make the AAD lidar backscatter match that measured by the ceilometer in below-cloud precipitation. The orange line in Fig. S1 shows the daily median of k_{tr}, including only periods where clouds are not fully or heavily attenuated where k_{tr} was used. The broad pattern is similar, with the calibration coefficient drifting upward until August, at which point there is a sizeable reduction with some recovery in late October. The similarity gives us some confidence that corrections are reasonable.

Rather than simply relying on either individual approach, the flowchart in Fig. S2 shows how the O'Connor and transfer calibrations are merged. When a fully or heavily attenuating cloud is present, the O'Connor estimate is used (left side of flowchart), and otherwise we compare the O'Connor calibration coefficient (which has been applied to a lightly attenuating cloud) to the k_{tr}. When $k'_{OConnor}$ (the prime denotes lightly attenuating) and k_{tr} match within a factor of 1/3, we simply use the average of the two as the estimated calibration factor. If they do not match, then we use average of the daily median of fully/heavily attenuating $k_{OConnor}$ coefficients (labeled k_{median} in the flowchart) and $k'_{OConnor}$. Ultimately, we found using averages (rather than k_{tr} alone or k_{median} alone) resulted in most accurately identifying the phase of cloud base correctly as liquid for warm clouds (CTT > 0°C). Nonetheless, a small fraction (5.8%) of the cases with light attenuation yields unphysical integrated attenuated backscatter ($\gamma < 0.02$ sr^{-1} or $\gamma > 0.2$ sr^{-1}). In these cases, we found defaulting to $k'_{OConnor}$ worked better than averaging with k_{tr} or k_{median}), such that only ~0.6% (1.1% in AM, 0.6% in JJA and 0.2% in SON) had unphysical values and were removed from the analysis (included in the "missing/bad data" fraction reported in Table #2 column 3).

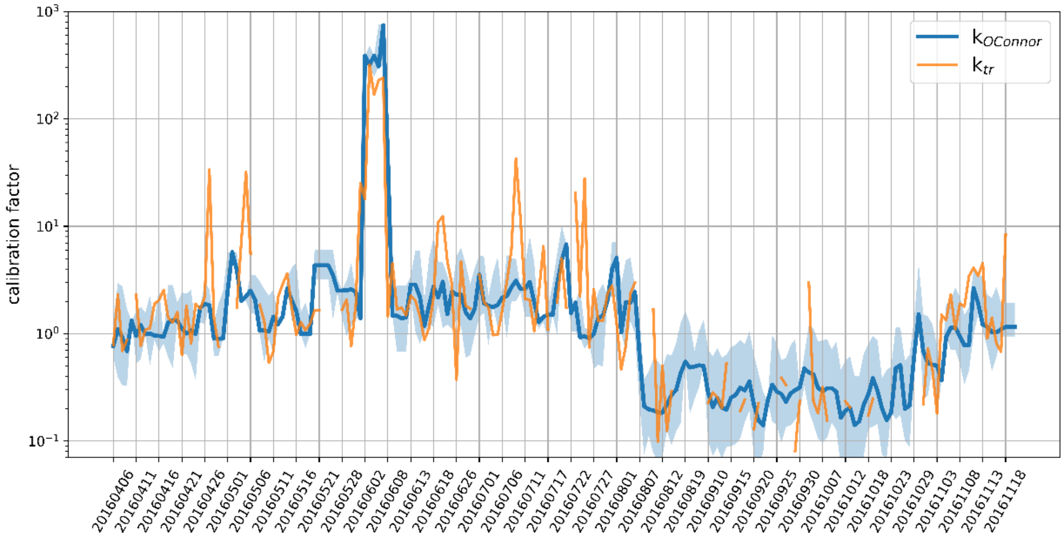

Figure S1: Time series of calibration coefficients calculated with the O'Connor method and subsequent filtering. The solid blue line represents the daily median, shading shows the daily range in calibration coefficients. The orange line is the daily median of transfer calibration coefficients; discontinuities in the orange line indicate where the transfer calibration was not applicable.

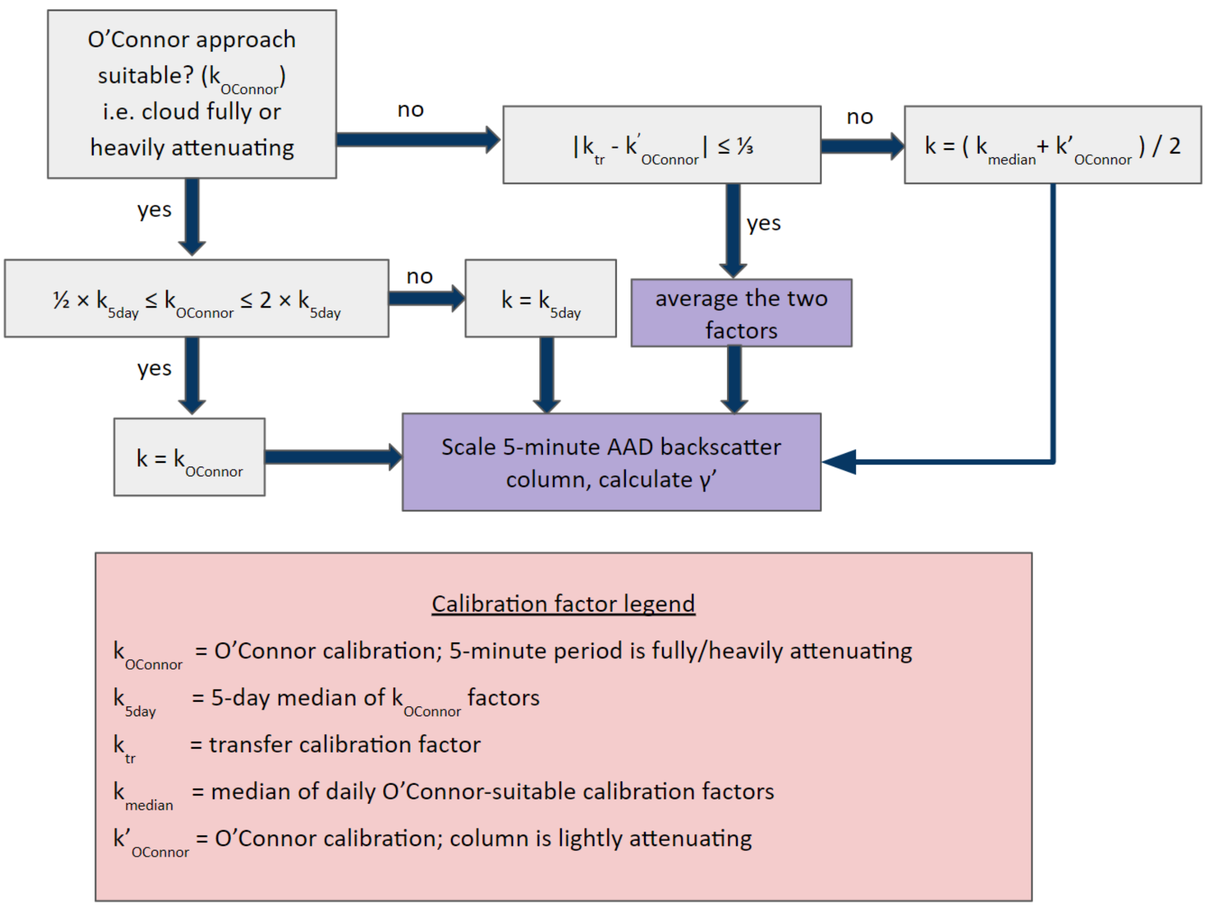

Figure S2: Flow chart of conditions to determine what calibration coefficient is used to scale the 5-minute lidar backscatter.

S2. Polarization lidar depolarization ratio calibration

The depolarization ratio, the ratio of the cross-to-co-polar backscatter (δ_L), also required a recalibration between August and October. As explained in Section S1, the original calibration was based on data collected in the May timeframe. The original AAD data contain an abrupt increase in the cross-polarization channel counts in August-October, resulting in a sizeable increase in δ_L (Fig. S3). The left panel of Fig. S3 shows a time series of δ_L for the below-cloud precipitation falling from warm-topped clouds in the original data. For light precipitation (where multiple scattering has little impact), we expect δ_L to be near-zero since spherical droplets should generate little to no cross-polarization. As the left panel shows, much of the time the below-cloud precipitation δ_L is near zero, until August and September (denoted by the red box). Note that Fig. S3 includes all below-cloud precip from warm clouds, not just light precipitation. Oddly, the depolarization ratio and (not shown) the cross-polarized backscatter return to pre-August levels near the beginning of November.

Taking the ratio of the mean cross-polarization counts before August during well-calibrated periods (6.8 counts) and during the period with elevated cross-pol from Aug.-Oct. (24 counts), we find a correction factor of 0.28. The resulting time series (right panel) after scaling by 0.28 during the bad period is shown in the right panel.

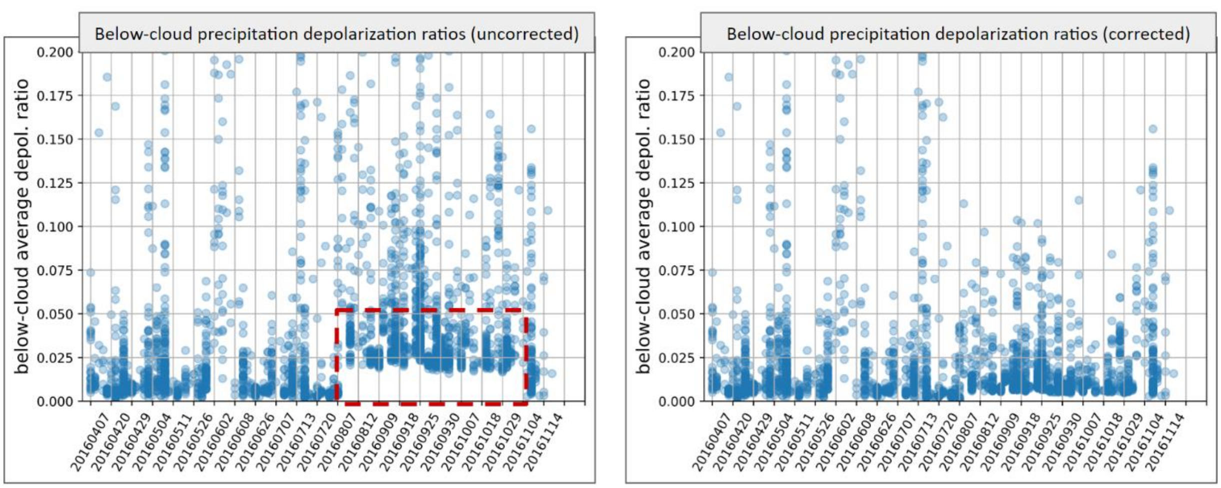

Figure S3: Time series of below-cloud depolarization ratios for warm-topped clouds before (left) and after (right) the calibration correction factor is applied. The red dashed box calls out the period where, due to an instrument malfunction, a step occurred in the cross-polarization channel counts, resulting in artificially raised depolarization ratios. The right plot is the depolarization time series after scaling the step by 0.28.